Optimal Integration Schemes for Polygonal Finite Element Method and eXtended Finite Element Method with Isotropic Homogenious and Polycrystaline Material

A Project Report

Submitted in partial fulfilment of the

requirements for the Degree of

Master of Engineering

in

Aerospace Engineering

by

Subhendu Chakraborty

Department of Aerospace Engineering

Indian Institute of Science

BANGALORE – 560 012

June 2011

©Subhendu Chakraborty

June 2011

All rights reserved

TO

My Teachers

Acknowledgements

I express the deepest gratitude to my supervisor, **Prof. D. Roy Mahapatra**, who has guided me throughout this project with his brilliant ideas whilst allowing me the freedom to work in my own way. His energy and enthusiasm always motivated me whenever I found myself in difficult situations. It was his Smart Material and Structure course that motivated me to take him as my guide in the ME Project. Without his guidance and encouragement the thesis would not have been completed.

I would like to thank **Prof. M.S. Bhat**, Chairman, Department of Aerospace Engineering for providing me excellent work environment. I also thank the faculty members of the Aerospace department and other departments in Indian Institute of Science from whom I had the privilege to learn many concepts and fundamentals which proved to be very valuable during this project.

I would like thank my classmates, lab mates and friends and particularly Satyendra Singh and Ahish who have been a great help whenever I got snagged in some conceptual problem or computational difficulties.

In addition I would like to thank, Sundararajan Natarajan, Phd scholar, Cardiff University, Wales, U.K and Stéphane Bordas, Professor, Cardiff University, Wales, U.K for constantly being in touch through emails and providing support whenever needed.

I would also like to thank my parents who have always taught me to follow my heart no matter what obstacles I might encounter. I am greatly indebted to them for their unconditional support and encouragement all through my life.

Publication from this work

1. Satyendra Singh, S. Natarajan, S. Chakraborty, D. Roy Mahapatra, Stéphane P.A. Bordas, Optimal numerical integration schemes for polygonal finite elements. *International Journal for Numerical Methods in Engineering* 2011; (under review)

2. S. Chakraborty, D. Roy Mahapatra, S. Natarajan and Stéphane P.A. Bordas, Polygonal XFEM for modelling deformation of polycrystalline microstructures. *International Conference on Extended Finite Element Methods - XFEM 2011*;

3. S. Chakraborty, S. Singh and D. Roy Mahapatra Modelling Polycrystalline Microstructures using Polygonal Finite Elements. *International Conference on Structural Mechanics and Reactor Technology -2011*

4. K. L. Singh, S. Chakraborty and D. R. Mahapatra Convergence of Fracture Parameter and Simulation of Crack Growth in XFEM. *XVII National Seminar on Aerospace Structures(NASAS)* 2011

Contents

List of Tables

List of Figures

Abstract

This thesis presents the implementation of Polygonal Finite Element Method(PFEM) in polycrystalline types of material. For polycrystalline material the crystallographic axis varies from grain to grain causing inhomogeneity. In this thesis to simulate the polycrystalline types of material each element has been considered as the polycrystalline grain and assigned arbitrary crystallographic orientation. For numerical integration the scheme developed by Satyendra et al. [45] has been verified for some simple cantilever beam type benchmark problems and compared with other numerical integration scheme(e.g. triangulation scheme, generalised gauss quadrature scheme and SC midpoint scheme). Then the above mentioned scheme has been implemented after modifying it by placing some additional integration points near the element boundary to incorporated the effect of material property variation across the element boundary. Such material property variation across grain boundary in a real pocrystaline material is related to what is known as grain boundary width in material science. Since exact solution for this type of problem is not possible, so strain energy has been computed and compared between two approaches of meteria modelling, one is without incorporating the polycrystaline effect i,e material is homogenious throughout the beam and another is incorporating the polycrystalline efect by assigning element wise arbitrary orientation of crystallographic axis. Results show the relative high strain energy and deflection when modelled as pollycrystalline material which clearly indicates the influence of crystallographic orientation on the behaviour of the beam. In this context of optimal integration scheme, discussed above, has been implemented in a framework to simulate crack based on XFEM. Edge crack and oblique crack have been used and the SIF values have been compared with the semi analytical solution,

which shows good convergence in SIF values. Next results are obtained for crack propagation. Edge crack and oblique crack have been considered and the propagation path has been studied for mesh with 4 node quadrilateral and 6 node hexagonal element.For each of the two types of crack, propagation path shows the mesh independency in the solution process.

Keywords

Polygonal Finite Element, Shawarz-Christoffel conformal Mapping, Extended Finite Element Method, Wachspress shape function, Numerical integration, Crack, J-integral, Stress intensity factor, crack propagation, polycrystaline material.

Chapter 1

Introduction

1.1 Polygonal Finite Element Method for Polycrystalline Material

Most of the problems in engineering is governed by some basic law of physics and using these basic laws it is possible to formulate those problems in terms of some partial differential equation called Governing Differential Equation(GDE). But in most of the cases it is not possible to solve those GDE's exactly mainly due to complicated geometry and boundary condition. And also, so far requirement of accuracy is concerned in engineering related problem, it is not necessary to have the exact solution of those problem. Finite Element Method(FEM) is a powerful numerical method to solve these partial differential equations. And has been widely used in the industry. But almost all commercial FEM packages uses either triangulation or quadrilateral element to discretize the domain. This is mainly due to the non availability of the efficient quadrature rule for numerical integration in polygonal domain. But it is not always possible to discretization a complicated geometry using only triangular or quadrilateral elements and also since most of the structural materials are polycrystalline in nature so for the modelling of the microstructure of those materials polygonal element provide great opportunity. Wachspress [11] proposed the construction of basis function on convex polygons for any number of

edges. After that significant advances have been made towards construction of barycentric coordinates over arbitrary polygons [12, 13]. A simplified expression for Wachspress basis functions is presented by Meyer *et al.* [14]. Floater [15] derived barycentric coordinates in which a vertex in a planar triangulation is expressed as a convex combination of its neighboring vertices. In Refs. [13] and [16], natural neighbor interpolation is used to construct C^0 shape functions on polygonal elements. The construction of polygonal interpolants using the principle of maximum entropy is described in Ref. [17]. Despite all the advantages, use of polygonal elements poses one difficulty similar to meshfree methods [18] and XFEM. Since the approximation functions for polygons are usually non-polynomial, numerical integration becomes a problem. Several schemes have been proposed to integrate this kind of approximation over polygonal domains to obtain the stiffness matrix. One such scheme is to map a polygon in physical space to a regular polygon [13, 16]. This regular polygon is then divided into triangles. These triangles are then mapped to reference triangle and numerical quadrature rules over triangle are used for numerical integration [19]. Hence two levels of mapping are required in this scheme. Natarajan *et al.* [20] proposed mapping of an arbitrary polygon to a unit-disk using Schwarz-Christoffel conformal mapping and used a mid-point integration [21] rule to integrate stiffness terms over a polygonal element. This method eliminates the need for two-level mapping involving isoparametric polygonal mapping and triangulation. However, the method still suffers from two existing disadvantages. First of all it is expensive to compute the Schwarz-Christoffel map for each polygon. And secondly a large number of integration points, around 20 or more, are required to get accurate results of numerical integration while using the mid-point integration rule. According to the mid-point integration rule, the integration points are placed at the centroid of each polar segments of the polygon. However, a significant improvement on element performance was proved in Ref. [20] and more needs to be done.

1.2 Extended Finite Element Method and Propagation of Crack

Finite element method has been used in fracture mechanics applications. Chan *et al.* [1] have shown the usefulness of finite element method in computation of crack tip stress intensity factors. Li *et al.* [2] compared two different methods for the calculation of energy release rates. However in all the conventional finite element methods, the mesh should conform to crack geometry. This imposes a major constraint on meshing and remeshing in case of crack growth problems. Babuska *et al.* [43] proposed a new type of finite element method called Partition of Unity Method (PUM). The method introduced the ability to include in the finite element space knowledge about the partial differential equation being solved by including the local enrichment functions in the finite element approximation. Later on this concept of the PUM is utilized to represent the arbitrarily oriented crack within the finite element mesh by means of enrichment functions [3, 4]. This method later came to be known as eXtended Finite Element Method (XFEM) [5]. The XFEM has been implemented in the polygonal framework [44]. In Polygonal XFEM, similar to XFEM on quadrilateral meshes, due to the presence the discontinuous enrichment functions and high strain gradient regions near crack tips special care has to be taken while numerically integrating the weak form of governing equation. The standard Gauss quadrature cannot be applied in elements enriched by discontinuous terms, because the Gauss quadrature implicitly assumes a polynomial approximation. This problem is overcome by partitioning the elements into subcells aligned to the discontinuity surface, in which the integrands are continuous and differentiable.Natarajan *et al.* [6] presented a method where strong and weak discontinuities could be integrated without dividing the elements into large number of sub-cells. Smoothed Finite Element Method (SFEM) combined with XFEM has also been used as one of the solutions to this problem [7]. The SFEM relies on strain smoothing, which was proposed by Chen *et al.* [8] for meshless methods. Natarajan *et al.* [9] proposed a new method by coupling the SFEM with the XFEM, a new numerical method called the Smoothed eXtended Finite

Element Method (SmXFEM).

Torsten *et al.* [54] has studied the crack propagation in polycrystalline material but usin the convention al FEM and each plygonal grain has been deviden in several numbers of triangle causing the method computationally inefficient. Tabarraei *et al.* [44] applied the XFEM method in polygonal framework. In order to obtain the numerical integration of the weak form for governing differential equation they subdivided the enriched elements into triangles. Then they used well known quadrature rules for triangle for numerical integration. Since no well established method exists for integrating over polygonal elements they used the triangulation scheme for unenriched elements too. This however requires huge computational resources.

1.3 Scope of this Thesis

Following goals have been achieved in this work,

1. The noble integration scheme proposed by Satyendra *et al.* [45] has been varified for few benchmark type cantiliver beam problems for which the exact solution is readily available. Strain energy and the error in dispacement norm has been calculated using different types of element(4 node quadrilateral, 5 node pentagonal and 6 node hexagonal) and under h-refinement. Satisfactory convergence has been achieved in strain energy calculation and error in displacement norm.

2. The above mentioned scheme with few modification has been used for polycrystalline types of problem and relative difference in strain energy and deflection shape has been studied for a homogeneous and a polycrystalline material under different types of meshing.

3. The same integration scheme has been used in XFEM framework to study the crack related problem. Few benchmark types of problem for which semi analytical solution is available has been studied. SIF values have been computed and compared

with the semi analytical solution which shows good convergence in SIF values upon h-refinement. High stress concentration near the crack tip has also been obtained.

4. At the last, the study of crack propagation has been done for mode-I and mixed mode crack problem by predicting the crack path using different types of element for meshing. In both the cases the resemblance in the predicted crack path shows the mesh independency on the solution process.

The outline of this thesis is as follows. In chapter 2 formulation of polygonal finite element method is presented. The basic equations of linear elasticity are revisited in section 2.1. We will briefly recall the formulation and the construction of polygonal finite elements in section 2.2 and discuss the construction of Wachspress shape functions in section 2.3. We discuss the numerical integration of weak form of governing equation in section 2.4 and give brief introduction to Schwarz-Christoffel mapping in section 2.5 and proposed integration scheme is discussed next. In chapter 3 we discuss the two-level mapping and propose two different optimization schemes of numerical integration. Few benchmark problems for comparison of results are considered next. Conventional triangulation scheme, SC mid-point method and generalized gauss quadrature(only for hexagonal discretization) have been used to compare the performance of the proposed two optimal integration schemes. Results are compared for structured as well as unstructured meshes with quadrilaterals, pentagons and hexagons. In chapter 4 the above mentioned integration scheme with the modification of few additional integration points near the element boundary has been used to study the same beam problem but considering the material as polycrystaline in nature by assigning element wise arbitrary principle material axis orrientation. In Chapter 5 we give the formulation of XFEM for crack problems. Section 5.1 briefly revisits basic equations of linear elasticity for crack problems. Section 5.2 discusses the crack modeling using discontinuous enrichment. Implementation of optimal integration scheme for extended finite element method is considered in section 5.3. Numerical examples are presented in Section 5.4. Next chapter 6 has been devoted to study the propagation of crack under mode-I and mixed mode condition which is followed by conclusions in chapter 7.

Chapter 2

Problem Formulation

2.1 Governing Equations and Weak Form

The governing equilibrium equations for a two-dimensional linear static elasticity problem defined in the domain Ω bounded by Γ and $\Gamma = \Gamma_u \cup \Gamma_t$, $\Gamma_u \cap \Gamma_t = \phi$ is given by

$$\nabla_s^{\mathrm{T}} \boldsymbol{\sigma} + \mathbf{b} = \mathbf{0} \quad \text{in } \Omega \tag{2.1}$$

where $\mathbf{0}$ is a null vector, $\boldsymbol{\sigma}$ is the stress tensor and $\mathbf{b}$ is the vector of external forces. The boundary conditions can be expressed as

$$\mathbf{u} = \overline{\mathbf{u}} \text{ on } \Gamma_u \tag{2.2}$$

$$\mathbf{n}^T \boldsymbol{\sigma} = \overline{\mathbf{t}} \text{ on } \Gamma_t \tag{2.3}$$

where $\overline{\mathbf{u}} = (\overline{u}_x, \overline{u}_y)^T$ is the prescribed displacement vector on the essential boundary Γ_u;
$\overline{\mathbf{t}} = (\overline{t}_x, \overline{t}_y)^T$ is the prescribed traction vector on the natural boundary Γ_t; $\mathbf{n}$ is the unit outward normal vector. The discrete equations for this problem are generated using the Galerkin weak form

$$\int_{\Omega} (\bigtriangledown_s \delta\mathbf{u})^T \mathbb{D} (\bigtriangledown_s \mathbf{u}) d\Omega - \int_{\Gamma} (\delta\mathbf{u}^T)\mathbf{b} d\Omega - \int_{\Gamma} (\delta\mathbf{u})^T \bar{\mathbf{t}} d\Gamma = 0 \tag{2.4}$$

where $\mathbf{u}$ and $\delta\mathbf{u}$ are the test functions that belong to admissible functions from Sobolev space and $\mathbb{D}$ is the constitutive matrix. The finite element method uses the following trial functions $\mathbf{u}^h(\mathbf{x})$ and the test functions $\delta\mathbf{u}^h(\mathbf{x})$:

$$\mathbf{u}^h(\mathbf{x}) = \sum_{i=1}^{N_P} \mathbf{N}_i(\mathbf{X})\mathbf{u}_i, \quad \delta\mathbf{u}^h(\mathbf{x}) = \sum_{i=1}^{N_P} \mathbf{N}_i(\mathbf{X})\delta\mathbf{u}_i \tag{2.5}$$

where N_P is the total number of nodes in the mesh.

$$\mathbf{N}_i = \begin{bmatrix} N_i & 0 \\ 0 & N_i \end{bmatrix} \tag{2.6}$$

is the shape functions matrix with entries being a polynomial of degree p or a rational polynomial associated with node i, $\mathbf{u}_i = [u_i, v_i]^T$ are the degrees of freedom associated with node i. By substituting the approximations $\mathbf{u}^h$ and $\delta\mathbf{u}^h$ into the weak form and invoking the arbitrariness of virtual nodal displacements, Equation (2.4) yields the standard discretized algebraic system of equations:

$$\mathbf{K}\mathbf{u} = \mathbf{f} \tag{2.7}$$

with the stiffness matrix given by

$$\mathbf{K} = \int_{\Omega^h} \mathbf{B}^\mathbf{T}\mathbf{D}\mathbf{B} d\Omega \tag{2.8}$$

and the load vector given by

$$\mathbf{f} = \int_{\Omega^h} \mathbf{N}^\mathbf{T}\mathbf{b} d\Omega + \int_{\Gamma_t} \mathbf{N}^\mathbf{T}\bar{\mathbf{t}} d\Gamma \tag{2.9}$$

where Ω_h is the discretized domain, formed by the union of elements Ω_e. The stiffness matrix $\mathbf{K}$ is symmetric, positive definite and with a strain-displacement matrix defined

as

$$\mathbf{B}_i(\mathbf{x}) = \bigtriangledown_s N_i(\mathbf{x}) = \begin{bmatrix} \frac{\partial N_i}{\partial x} & 0 \\ 0 & \frac{\partial N_i}{\partial y} \\ \frac{\partial N_i}{\partial y} & \frac{\partial N_i}{\partial x} \end{bmatrix} \tag{2.10}$$

where i in equation (2.10) corresponds to node i of the element. The size of the $\mathbf{B}$ matrix depends on the number of nodes in a polygonal element. In this thesis we consider the nodes only at the vertices of the polygonal elements.

2.2 Approximations on Polygons

Consider a polygonal domain $\Omega \subset \mathbb{R}^2$ that is described by n nodes. Let the i^{th} node be denoted as p_i and the coordinate of the node i is $\mathbf{x}_i = (x_i, y_i)$. Any generic point p with coordinate $\mathbf{x} = (x, y) \in \Omega$, has a set of associated shape functions $\phi_i(\mathbf{x})$. An approximation scheme for a scalar valued function $u : \Omega \to \mathbb{R}$ can be written as

$$u^h(\mathbf{x}) = \sum_{i=1}^{n} \phi_i(\mathbf{x}) u_i \tag{2.11}$$

where u_i are the unknown nodal variables at n vertices (nodes) of the polygon. From the viewpoint of a conforming Galerkin approximation, the following are some of the desirable properties of shape functions and of the resulting approximation:

1. Form a partition of unity to assure constant consistency condition, and that $\phi_i(\mathbf{x})$ is non-negative and bounded:

$$\sum_{i=1}^{n} \phi_i(\mathbf{x}) = 1, \quad 0 \leq \phi_i(\mathbf{x}) \leq 1 \tag{2.12}$$

2. Interpolate nodal data:

$$\phi_i(\mathbf{x}_j) = \delta_{ij} \tag{2.13}$$

where δ_{ij} is the Kronecker-delta. It ensures that the interpolated field at a node is identical to the nodal quantity: $u^h(\mathbf{x}_i) = u_i$.

3. Linear precision or linear completeness:

$$\sum_{i=1}^{n} \phi_i(\mathbf{x})\mathbf{x}_i = \mathbf{x} \tag{2.14}$$

   From this property it can be concluded that the shape function can exactly reproduce a linear function.

4. On the boundary of the domain Ω, the interpolant must be precisely linear, i.e. interior shape functions should not contribute if a point p lying on the convex hull and in addition only the nodes adjacent to point p must have non-zero values so that a linear interpolant is realized:

$$u^h(t) = \alpha u_1 + (1-\alpha)u_2, \;\; \mathbf{x} = \alpha \mathbf{x}_1 + (1-\alpha)\mathbf{x}_2, \;\; \mathbf{x} \in \partial\Omega, \;\; \alpha \in [0,1]. \tag{2.15}$$

Equation (2.15) in conjunction with the Kronecker-delta property in equation (2.13) ensures that essential boundary conditions can be imposed. The following methods can be used to build shape functions on polygonal domain.

1. Shape functions using length and area measures [11, 13, 16, 22] (e.g. Wachspress shape function, Metric coordinate, Rational Polynomial)
2. Natural neighbor shape functions [23, 24]
3. Maximum entropy approximation [17, 25, 26, 27, 28]
4. Barycentric coordinates on irregular *n-gon* [14, 29]

In this thesis Wachspress shape functions are used to construct interpolation function.

2.3 Wachspress Shape Functions

Using the principles of projective geometry, Wachspress constructed rational basis functions on polygonal domain [11]. In general, for an n-sided convex polygon, a Wachspress

shape function $N_i^{(n)}(x, y)$ is a polynomial of the following form:

$$N_i^n(x, y) = \frac{\mathcal{P}^{n-2}(x, y)}{\mathcal{P}^{n-3}(x, y)} \tag{2.16}$$

where $\mathcal{P}^{(m)}(x, y)$ is an m-degree polynomial in (x, y). In Ref. [14], a simple expression have been obtained for Wachspress's basis functions which can be expressed as

$$\phi_i^w(\mathbf{x}) = \frac{w_i(\mathbf{x})}{\sum_{j=1}^n w_j(\mathbf{x})} \tag{2.17a}$$

$$w_i(\mathbf{x}) = \frac{A(p_{i-1}, p_i, p_{i+1})}{A(p_{i-1}, p_i, p)A(p_i, p_{i+1}, p)} = \frac{\cot\gamma_i + \cot\delta_i}{||\mathbf{x} - \mathbf{x}_i||^2} \tag{2.17b}$$

where the last expression is due to Meyer *et al.* [14]. In equation (2.17), $A(a, b, c)$ is the

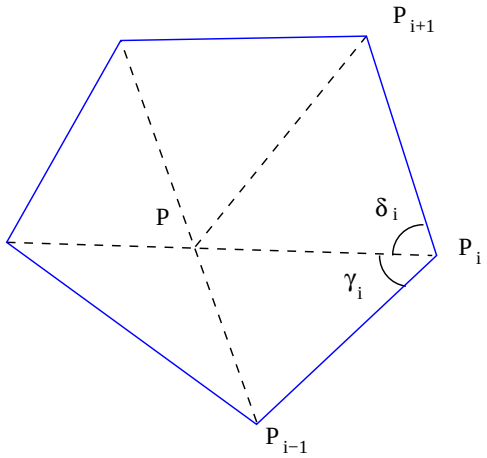

Figure 2.1: Barycentric coordinates: Wachspress basis function('P' is any point inside the polygon).

signed area of triangle $[a, b, c]$ and γ_i and δ_i are shown in figure 2.1. The signed area of a triangle whose vertices A_i have coordinates (x_i, y_i), for $1 \leq i \leq 3$, is given by [30]

$$A = \frac{1}{2}\begin{vmatrix} x_1 & y_1 & 1 \\ x_2 & y_2 & 1 \\ x_3 & y_3 & 1 \end{vmatrix} = \frac{1}{2}\left[x_3\left(y_1 - y_2\right) - y_3\left(x_1 - x_2\right) + x_1y_2 - y_1x_2\right] \tag{2.18}$$

In this thesis Wachspress shape functions are constructed by substituting the signed

area of the triangle given by equation (2.18) in equation (2.17b). The Wachspress shape functions are the functions of minimal degree that satisfy boundedness, linearity and linear dependence on convex polyshapes [31]. Figure 2.2a, figure 2.2b and figure 2.2c shows the shape of the wachpress basis function on quadrilateral, pentagonal and hexagonal convex domain respectively.

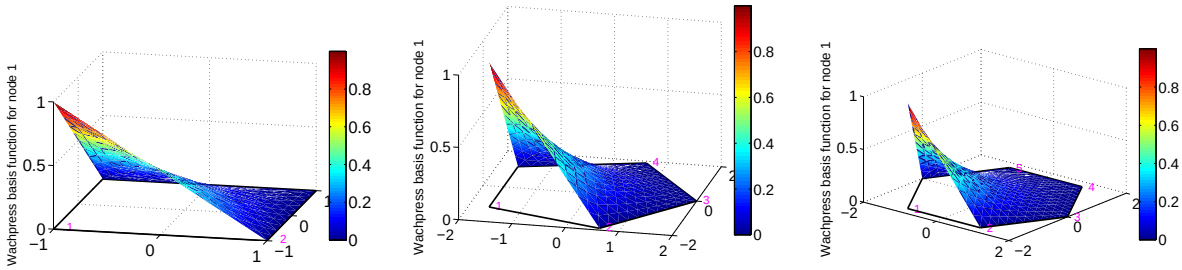

(a) (b) (c)

Figure 2.2: Shape of Wachpress basis function. (a) Quadrilateral domain. (b) Pentagonal domain. (c) Hexagonal domain.

2.4 Numerical Integration of Weak Form

The element stiffness matrix in equation (2.8) must be evaluated over the element. In the standard polynomial finite element method, an element does not have more than four edges for 2D domains. Therefore, the Gauss quadrature rule for polynomials, which is optimal, can effectively be used to integrate the weak forms. To integrate weak forms over the *n-gon*, no general quadrature rules are available which are proved to be optimal for the integrals present in the stiffness matrices . The following methods can be used for the integration of the weak form over the *n-gon* element.

1. Sukumar and Tabarraei [13] have proposed a method to integrate the weak form over a *n-gon* element. In this method a physical element is mapped to a canonical domain and then that canonical element is subdivided into triangles and well known rules are applied on each triangle for numerical integration. This method involves a two-level isoparametric mapping: Physical element (Ω_e) $\rightarrow$ Reference

polygon (Ω_o) $\rightarrow$ Triangle. The standard triangular quadrature rule is used for integration over the triangle. Moreover, in isoparametric mapping, length measures are preserved, but not the included angles, and so the positivity of the Jacobian needs to be ensured. To ensure the positivity of the Jacobian the element should be a convex element.

2. Another method to integrate over the *n-gon* element is the Smoothed Finite Element Method (SFEM) [32] which is based on strain smoothening introduced by Chen *et al.* [33] for mesh-free methods. The extension of strain smoothening to finite element method leads to integration on boundary of the finite elements, which avoids the requirement of isoparametric mapping. Even in case of the SFEM, the *n-gon* element is subdivided into triangles, solely for the purpose of numerical integration. Unlike in the triangulation scheme, in SFEM the integration points lie on the boundary of the triangles. It was shown in Ref. [34] that Wachspress interpolant can be used to construct SFEM approximations in physical space.

3. The other method to integrate over the *n-gon* element is the method developed by Natarajan *et al.* [20]. In this method an *n-gon* element is mapped to a unit-disk using Schwarz-Christoffel conformal mapping and various cubature rules are applied for integration.

4. Recently Mousavi *et al.* [35] proposed a numerical algorithm based on group theory and numerical optimization to compute efficient quadrature rules for integration of bivariate polynomials over arbitrary polygons. They have shown that for the integration involving rational polynomial shape functions over a regular hexagon their quadrature rule requires as high as 85 integration points for a relative error of 10^{-8}.

In this thesis new method is proposed by considering the optimality of the integration points with respect to the resulting integral in the stiffness matrix. This method is described in section 2.6. In this proposed method Schwarz-Christoffel mapping is

done using SCPACK [36] subroutines in FORTRAN and MATLAB SC Toolbox [37] in MATLAB.

2.5 Schwarz-Christoffel Conformal Mapping (SCCM)

Let P be the interior of a polygon Γ having vertices $w_1, ..., w_n$ and interior angles $\alpha_1\pi, ..., \alpha_n\pi$ in the counter-clockwise order. Let f be any conformal map from the unit-disk to P. Then, the Schwarz-Christoffel formula for a disk is given by [38]

$$f(z) = A + C \int^{z} \prod_{k=1}^{n} \left(1 - \frac{\zeta}{z_k}\right)^{\alpha_k - 1} d\zeta \tag{2.19}$$

for some complex constants A and C, where $w_k = f(z)\ for\ k = 1, ..., n$. The SCCM integral in equation (2.19), in general, have no exact solution and has to be solved numerically. All the necessary numerical steps are implemented using SCPACK FORTRAN library [36] and SCT Toolbox in MATLAB [37]. The Jacobian of the SCCM mapping is easily computed since the map is in an integral form and is given by

$$\frac{df}{dz} = \prod_{k=1}^{n} \left(1 - \frac{\zeta}{z_k}\right)^{\alpha_k - 1} \tag{2.20}$$

2.6 Numerical Integration

In this section we describe the proposed method of numerical integration. In this scheme an arbitrary polygon in the physical domain is first mapped to a non-dimensional reference polygon using isoparametric mapping. The non-dimensional reference polygon is a regular polygon with length of its edges 2 as depicted in figures 2.3b, 2.4b and 2.5b. Details regarding mapping from physical domain to non-dimensional domain (reference polygon) can be found in ref. [13]. The reference polygon is then mapped to a unit-disk using Schwarz-Christoffel (SC) conformal mapping. Further details regarding mapping

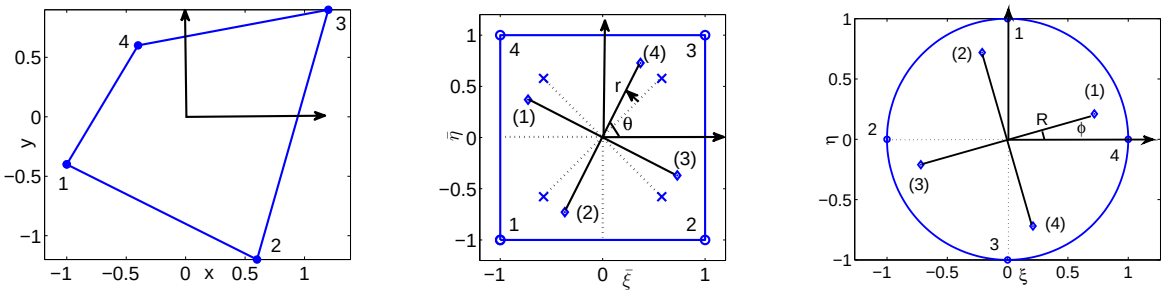

(a) (b) (c)

Figure 2.3: Two level mapping and placement of integration points for quadrilateral. Integration points are numbered and shown within parentheses. (a) Physical element. (b) Reference polygon. (c) Element mapped to unit-circle. Points connected by dotted lines in (b) are the original gauss points in standard isoparametric mapping.

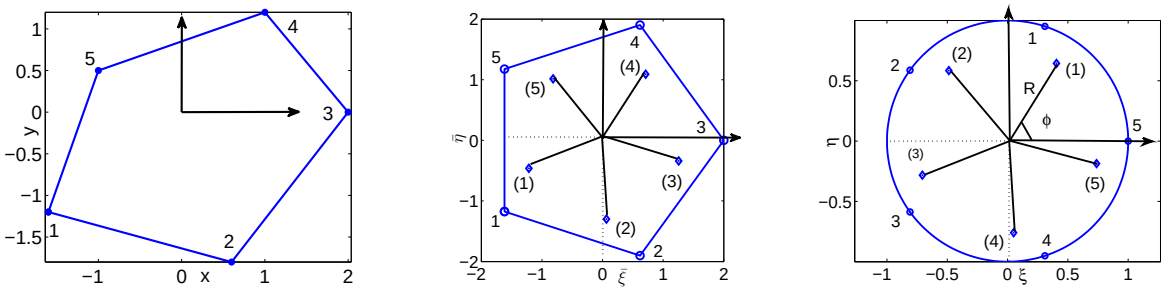

(a) (b) (c)

Figure 2.4: Two level mapping and placement of integration points for pentagon. Integration points are numbered and shown within parentheses. (a) Physical element. (b) Reference polygon. (c) Element mapped to unit-circle.

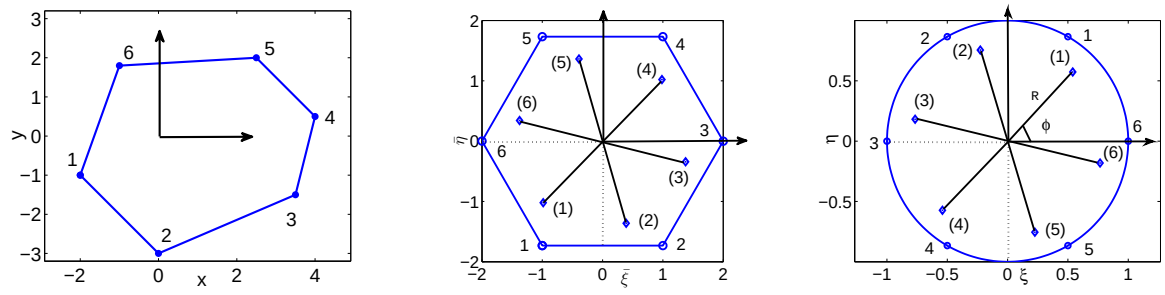

(a) (b) (c)

Figure 2.5: Two level mapping and placement of integration points for hexagon. Integration points are numbered and shown within parentheses. (a) Physical element. (b) Reference polygon. (c) element mapped to unit-circle.

from the polygon to the unit-disk can be found in ref. [20]. Figures 2.3, 2.4 and 2.5 show the two-level mapping for quadrilateral, pentagon and hexagon respectively. Integration points are defined over unit-disk. For the present case of two-level mapping the following approximation can be used to integrate $f(x, y)$ on an element in physical space:

$$\begin{aligned}\int_{\Omega} f(x,y)dxdy &= \int_{\Omega_p} f(\bar{\xi},\bar{\eta})J_{ip}d\bar{\xi}d\bar{\eta} \\ &= \int_{\Omega_c} f(\xi,\eta)J_{ip}J_{sc}d\xi d\eta \\ &\simeq \sum_{i=1}^{n_\theta}\sum_{j=1}^{n_r} A_{ij} f(r_j\cos\theta_i, r_j\sin\theta_i)\end{aligned} \tag{2.21}$$

where θ and r are the coordinates of integration points. A_{ij}'s are the weights associated with each integration point. Weight associated is the area of segment corresponding to that integration point. J_{ip} and J_{sc} are the Jacobians associated with isoparametric and SC mapping respectively. The schemes employed to find the optimum integration points for *n-gons* are discussed in the later sections of this thesis.

2.7 Validation Methodology

A two-dimensional cantilever beam subjected to shear and tensile loads at the free end is examined (Figure 2.6). The following geometry and material properties are used: length $L = 10$, height $D = 2$, thickness $t = 1$, Young's modulus $E = 7MPa$, Poisson's ratio = 0.3. A force of $100N$ is applied for shear and tensile loading cases.

The exact solution [39] for displacements and stresses for shear loading is given by

$$u(x,y) = \frac{Py}{6\overline{E}I}\left[(6L-3x)x + (2+\overline{\nu})\left(y^2 - \frac{D^2}{4}\right)\right] \tag{2.22a}$$

$$v(x,y) = -\frac{Py}{6\overline{E}I}\left[3\overline{\nu}y^2(L-x) + (4+5\overline{\nu})\frac{D^2x}{4} + (3L-x)x^2\right] \tag{2.22b}$$

where I is the second moment of inertia. Young's modulus and Poisson's ratio are,

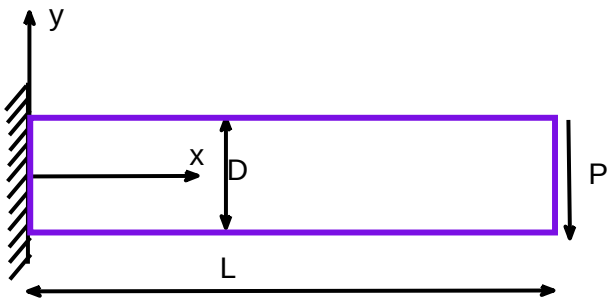

(a)

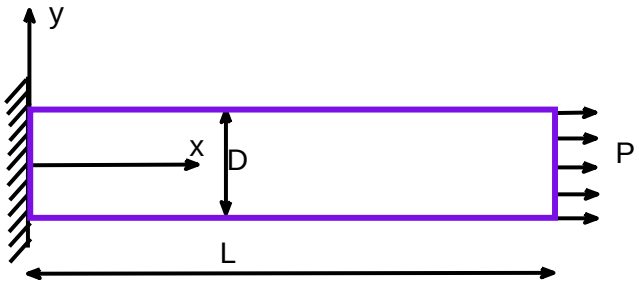

(b)

Figure 2.6: Finite element model with boundary conditions. (a) Pure shear. (b) Pure tension.

respectively

$$\overline{E} = \begin{cases} E \text{ (plane stress)} \\ \frac{E}{1-\nu^2} \text{ (plane strain)} \end{cases} \qquad \overline{v} = \begin{cases} \nu \text{ (plane stress)} \\ \frac{\nu}{1-\nu} \text{ (plane strain)} \end{cases} \tag{2.23}$$

Augarde *et al.* [40] discussed on the boundary conditions required for this exact solution given by equation (2.22). This solution holds only if the shearing forces on the ends are distributed according to the same parabolic law as the shear stress τ_{xy} and the intensity of the normal forces at the built-in end is proportional to y. Therefore the shear force at the end is applied according to the same parabolic law given by τ_{xy} as

$$\tau_{xy}(x,y) = -\frac{P}{2I}\left(\frac{D^2}{4} - y^2\right), \;\; \sigma_{xx}(x,y) = \frac{P(L-x)y}{I}, \;\; \sigma_{yy}(x,y) = 0 \tag{2.24}$$

The exact solution for displacements under tensile loading is given by

$$u(x) = \frac{\sigma}{E}x \tag{2.25a}$$

$$v(x,y) = -\nu\frac{\sigma}{E}xy \tag{2.25b}$$

As the problem is linear we can superimpose the displacement from axial and shear force to account for the case when both the shear and axial loading is applied on the beam. The above exact solutions for displacements are used to compute the error norms, as defined in section 3.1, for shear and tensile loading cases.

Chapter 3

Optimal Numerical Integration

This chapter discusses the proposed two schemes to determine the optimal location of integration points in polygon. One is based on the Frobenius norm and the other is based on the displacement error in infinity norm.

3.1 Global Error Measures

For the purpose of error estimation and convergence studies L_2 norm in interpolation field and energy norm are used. The L_2 norm of displacement error is given by

$$\|\mathbf{u} - \mathbf{u}_h\|_{L_2(\Omega)} = \sqrt{\int_\Omega \left[(\mathbf{u} - \mathbf{u}_h) \cdot (\mathbf{u} - \mathbf{u}_h)\right] d\Omega} \tag{3.1}$$

where $\mathbf{u}_h$ is the numerical solution and $\mathbf{u}$ is the analytical solution, or a reference solution. The energy norm is given by

$$\|\mathbf{u} - \mathbf{u}_h\|_{E(\Omega)} = \sqrt{\int_\Omega \left[(\boldsymbol{\varepsilon} - \boldsymbol{\varepsilon}_h)^T \mathbf{D} (\boldsymbol{\varepsilon} - \boldsymbol{\varepsilon}_h)\right] d\Omega} \tag{3.2}$$

The above norms plotted against the number of nodes to study the convergence as the mesh is refined.

3.2 Determination of Optimal Integration Points

In this section we discuss the methodology employed to obtain the optimal integration points for the quadrilateral, pentagonal and hexagonal elements. As explained earlier, the polygon in physical domain is mapped to non-dimensional coordinates first. For this the integration in equation (2.8) needs to be performed over the reference element domain. This is done by numerically mapping the reference element on to unit-disk by Schwarz-Christoffel conformal mapping and integrating it over this unit-disk. It is impossible to invert the map analytically. Any semi-analytical method of optimizing the Gauss points, as done in case of Gaussian quadrature for isoparametric mapping in quadrilateral element is not feasible in the present case. Therefore an attempt is made to determine the optimal integration points entirely numerically. In conventional isoparametric formulation, Gaussian quadrature gives the exact result for 4-node quadrilateral elements using 2×2 integration rule. Therefore we start only with four integration points in the present method for 4-node quadrilateral element and perform further optimization since we have SC mapping instead of isoparametric mapping on unit-disk. We also show that the present method, with just four integration points gives results comparable to that of isoparametric finite element. This was not possible earlier when a single step mapping using polygon → disk alone with Mid-Point integration scheme was used [20]. This is due to the fact that the Wachspress shape functions are defined over an arbitrary physical polygon, the resulting integrand will have different form for different arbitrary polygonal elements. Later we extend this optimization method to pentagons and hexagons using 5 and 6 integration points, respectively. Figures 2.3c, 2.4c and 2.5c show the location of integration points for quadrilateral, pentagonal and hexagonal elements symmetrically located over the unit-disk.

3.2.1 Optimal integration for polygonal elements: scheme 1

In scheme 1 first the stiffness matrix of the reference element using a known and accurate method, although computationally expensive, is calculated. This solution is referred to

as the reference solution. Now the integration points on unit-disk are placed as shown in figures 2.3c, 2.4c and 2.5c. Initial location of integration points is not important since the location of the integration points is optimized. Let (R, ϕ) be the polar coordinate of an integration point. The stiffness matrix is calculated by the method outlined in section 2.6. The stiffness matrix thus obtained is compared with the stiffness matrix obtained from the reference solution and the error in the stiffness matrix in terms of Frobenius norm of error matrix is calculated. The Frobenius norm of a matrix K is given by

$$\|K\|_F = \sqrt{\sum_{i=1}^{m}\sum_{j=1}^{n}|k_{ij}|^2} \tag{3.3}$$

The error in the stiffness matrix is defined as

$$E_k = \frac{\|K - K_h\|_F}{\|K\|_F} \times 100\ \% \tag{3.4}$$

where K and K_h are the stiffness matrices obtained from reference solution and the proposed solution method with optimised integration points, respectively. Now the values of R and ϕ are varied and error as defined in equation (3.4) is plotted over the entire domain. The value of R and ϕ corresponding to minimum error in E_k gives the optimal integration points. Scheme 1 is applied to quadrilateral (n=4), pentagon (n=5) and hexagon (n=6) and discussed in details in the later sections of this thesis.

3.2.2 Optimal integration for polygonal elements: scheme 2

Scheme 2 is based on minimizing the error in infinity norm of the the displacement. A single element patch test is used to obtain results independent of the mesh. The relative error in infinity norm of displacement is given by

$$E_\infty = \frac{\|\mathbf{u} - \mathbf{u}_h\|_\infty}{\|\mathbf{u}\|_\infty} \tag{3.5}$$

Now from equation (2.7)

$$\mathbf{u} = \mathbf{K}^{-1}\mathbf{f} \tag{3.6a}$$

$$\mathbf{u}_h = {\mathbf{K}_h}^{-1}\mathbf{f} \tag{3.6b}$$

By subtracting equation (3.6b) from equation (3.6a) we get

$$\mathbf{u} - \mathbf{u}_h = \left(\mathbf{K}^{-1} - {\mathbf{K}_h}^{-1}\right)\mathbf{f}$$

Now for the force of unit magnitude ($f = 1$) applied at all nodes (see fig. 3.3, 3.13 and 3.23), one has

$$\mathbf{u} - \mathbf{u}_h = \left(\mathbf{K}^{-1} - {\mathbf{K}_h}^{-1}\right)\mathbf{1} = \sum_j \left({\mathbf{K}_{ij}}^{-1} - {\mathbf{K}_{hij}}^{-1}\right) \tag{3.7}$$

where $\mathbf{1}$ is a vector whose all elements are unity. By taking maximum of absolute values over rows on both sides, we get

$$\max_{1\le i\le n} |\mathbf{u} - \mathbf{u}_h| = \max_{1\le i\le n} \left| \sum_j \left({\mathbf{K}_{ij}}^{-1} - {\mathbf{K}_{hij}}^{-1}\right) \right| \tag{3.8}$$

The left hand side in equation (3.8) is the infinity norm of vector $\mathbf{u} - \mathbf{u}_h$ and the right hand side is the infinity norm of matrix $\mathbf{K}^{-1} - {\mathbf{K}_h}^{-1}$. That is

$$\|\mathbf{u} - \mathbf{u}_h\|_\infty = \left\|\mathbf{K}^{-1} - {\mathbf{K}_h}^{-1}\right\|_\infty \tag{3.9}$$

The relative error in infinity norm is expressed as

$$\frac{\|\mathbf{u} - \mathbf{u}_h\|_\infty}{\|\mathbf{u}\|_\infty} = \frac{\left\|\mathbf{K}^{-1} - {\mathbf{K}_h}^{-1}\right\|_\infty}{\|\mathbf{K}^{-1}\|_\infty} = \frac{\left\|{\mathbf{K}_h}^{-1} - \mathbf{K}^{-1}\right\|_\infty}{\|\mathbf{K}^{-1}\|_\infty} \tag{3.10}$$

The right most expression in equation (3.10) gives the relative error in infinity norm of displacement in terms of stiffness matrices. This error in infinity norm of displacement vs. R and ϕ is plotted and the values of R and ϕ corresponding to minimum error give the optimal integration points. Scheme 2 is applied to quadrilateral (n=4), pentagon

(n=5) and hexagon (n=6) as discussed in the later sections of this thesis.

Now we further investigate the upper bound of error in infinity norm of displacement as given by equation (3.10). We frequently use norms to quantify the effect of perturbations. As an illustration of this, let us quantify the change in $\mathbf{K}^{-1}$ as a function of change in $\mathbf{K}$. Let us use error in stiffness matrix $\mathbf{E} = \mathbf{K}_h - \mathbf{K}$ as a perturbation in stiffness matrix $\mathbf{K}$. Now if $\mathbf{K}$ is non-singular and $\mathbf{r} \equiv \|\mathbf{K^{-1}E}\|_\infty < \mathbf{1}$, then $\mathbf{K} + \mathbf{E}$ is nonsingular and from the theorem given in Ref. [41]

$$\left\|(\mathbf{K}+\mathbf{E})^{-1} - \mathbf{K}^{-1}\right\|_\infty \leq \frac{\|\mathbf{E}\|_\infty \|\mathbf{K}^{-1}\|_\infty^2}{1-\mathbf{r}} \tag{3.11}$$

on rearranging the terms we get

$$\frac{\left\|(\mathbf{K}+\mathbf{E})^{-1} - \mathbf{K}^{-1}\right\|_\infty}{\|\mathbf{K}^{-1}\|_\infty} \leq \frac{\|\mathbf{E}\|_\infty \|\mathbf{K}^{-1}\|_\infty}{1-\mathbf{r}} \tag{3.12}$$

The left hand sides in equation (3.12) is the error in infinity norm of the displacement as given by equation (3.10) which involves computation of several matrix inversions. Its upper bound (for $E < 100\%$) can be computed more accurately since it involves computation of K^{-1} only once. The above gives good reliability in computing infinity norm error.

3.3 Analysis and Comparison of Results: Quadrilaterals (n=4)

The reference element is shown in figure 2.3b. It has been observed that the shape functions obtained for 4-node quadrilateral element are indeed the bilinear shape functions. Therefore we start with the same 2×2 Gauss integration points, which are optimal in isoparametric formulation. We then show that since we have SC mapping, these points are not the optimal points in the present case and later on we obtain the optimal integration points for the same by the two different schemes explained in sec. 3.2.1 and sec. 3.2.2.

3.3.1 Scheme 1 applied to quadrilaterals (n=4)

The integration points for quadrilaterals for 2×2 Gauss integration rules are shown in figure 2.3b and denoted by "×" markers. As discussed previously, we compute the error in Frobenius norm of stiffness matrix. An error of 28 % is found with the present 2×2 integration points. Hence these points are not optimal in the present case of SC mapping. We now represent integration points in polar coordinates r and θ. Then we vary the angle θ in small steps keeping the radius r constant at value equal to the radial distance of integration points in 2×2 Gauss rule. The coordinates of the integration points in the Cartesian coordinate system are calculated as

$$\bar{\xi}_i = r\cos\left(\theta + \frac{\pi}{2}(i-1)\right) \;;\; \bar{\eta}_i = r\sin\left(\theta + \frac{\pi}{2}(i-1)\right) \tag{3.13}$$

for the i^{th} integration point, where $1 \leq i \leq 4$. The stiffness matrix from an isoparametric formulation is used as reference solution. It is apparent that for every point $p(\bar{\xi}, \bar{\eta})$ in the quadrilateral there is a corresponding point $p(\xi, \eta)$ in the unit-disk. These points on the unit-disk are represented by R and ϕ in polar coordinates. The error in Frobenius norm vs. R and ϕ is plotted in Figure 3.1. The values of R and ϕ and hence r and θ corresponding to minimum error are given in table 3.1. These optimal integration points

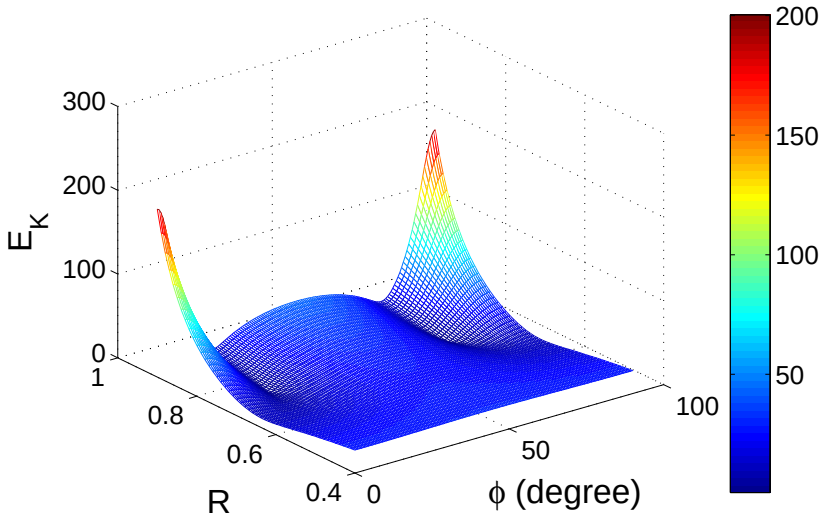

Figure 3.1: Error in Frobenius norm vs. coordinates (R, ϕ) of integration points on unit circle for 4-node quadrilateral element.

are shown in figure 2.3b and denoted by "$\diamond$" markers. To get these integration points we have used regular quadrilateral element in our error analysis. So it is needed to show the optimality of these integration points for unstructured element also. Figure (3.2) shows the almost invarient nature of these optimal integration points under various skewness angle.

Table 3.1: Optimal coordinate of integration points for 4-node quadrilateral element.

	In quadrilateral domain (fig. 2.3b)	In unit-disk domain (fig. 2.3c)
Min. error in Frobenius norm	$8 \times 10^{-4}\%$	$8 \times 10^{-4}\%$
$Radius_{opt}$	0.816496	0.749209
$Angle_{opt}$	63.086559^o	16.306493^o

A careful observation shows that the radial location of these integration points is the same as in 2×2 Gauss integration rules but they are now rotated by an angle of 18.086559^o. In fact rotation of 2×2 Gauss points by an angle of -18.086559^o also gives the same result.

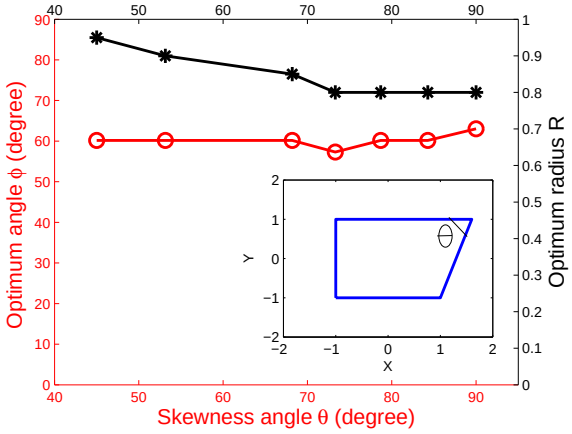

Figure 3.2: Variation of the optimal coordinate of the integration point (R, ϕ) for various skewness angle (θ) in the inset showing sensitivity to element shape.

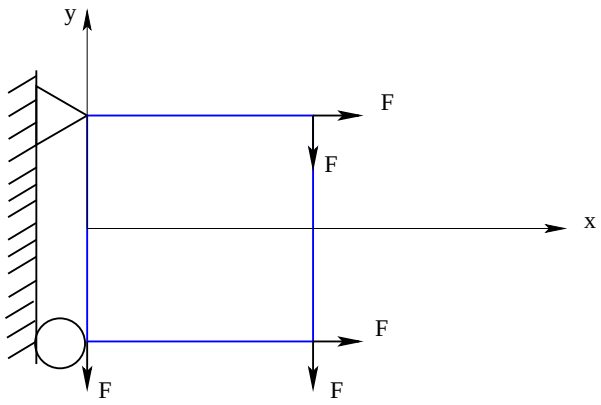

Figure 3.3: FE model with boundary conditions for scheme 2 based optimization for quadrilateral element.

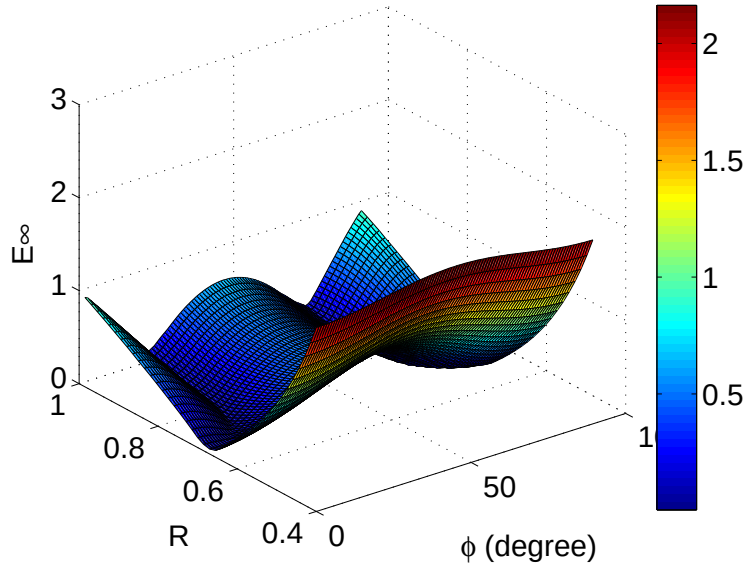

Figure 3.4: Error in infinity norm of u vs. coordinates (R, ϕ) of integration points on unit circle for 4-node quadrilateral element.

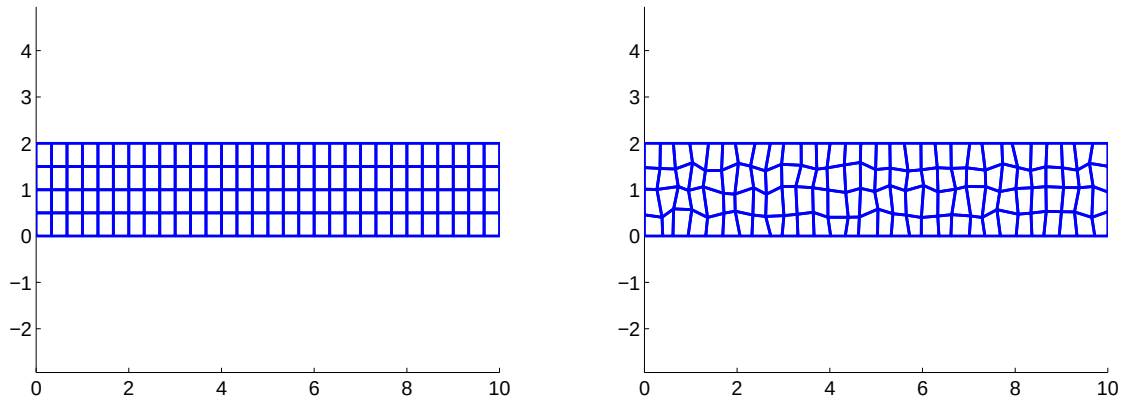

(a) (b)

Figure 3.5: (a) Structured mesh and (b) unstructured mesh with quadrilateral elements.

3.3.2 Scheme 2 applied to quadrilaterals (n=4)

Figure 3.3 shows the finite element model with essential and natural boundary conditions used for optimization using scheme 2 for 4-node quadrilateral element. The error in infinity norm of the displacement as given by equation (3.10) vs. R and ϕ is plotted in figure 3.4. The integration points thus obtained by scheme 2 for quadrilateral are found to be the same as those obtained by scheme 1 (table 3.1).

Figure 3.5 shows a typical structured mesh and an unstructured mesh with 4-node quadrilateral elements. Convergence in strain energy against the number of nodes for structured and unstructured mesh under pure tensile loading case is shown in figures 3.6a and 3.6b, respectively. The error in strain energy for SC mid-point method is 3.3 % with about 300 nodes whereas in case of the present method the error in strain energy is less than 0.2 % with 300 nodes for structured quadrilateral mesh. Similar results are observed for unstructured quadrilateral mesh too. Convergence in strain energy against the number of nodes for structured and unstructured mesh under pure shear loading case is shown in figures 3.7a and 3.7b, respectively. The convergence in strain energy against the number of nodes for structured and unstructured mesh under combined loading case is shown in figures 3.8a and 3.8b, respectively. The convergence rate for various cases are shown in inset in the corresponding figures.

The convergence in relative error in L_2 norm is plotted in figure 3.9 for pure tension case. In this case too the present method is much superior to SC mid-point method. For the tensile loading case the error in relative L_2 norm for the present method with 300 nodes is of the order of 10^{-3} and 10^{-2} for structured and unstructured meshes, respectively (figures 3.9a and 3.9b). Whereas the order of error in L_2 norm for the SC mid-point method even with 300 nodes is 10^{-1} for both structured and unstructured mesh. For the case of shear loading the error in L_2 norm is twice in case of the SC mid-point method than the error in case of the present method with 300 nodes (see figures 3.10a and 3.10b). Convergence in relative error in L_2 norm of displacement is plotted in figure 3.11 for combined loading case.

In comparison to the triangulation scheme , to achieve the same accuracy as we

have achieved using our scheme (i,e using only four integration points) the triangulation scheme need as much as fifty two integration points(i.e thirteen integration points per triangle).

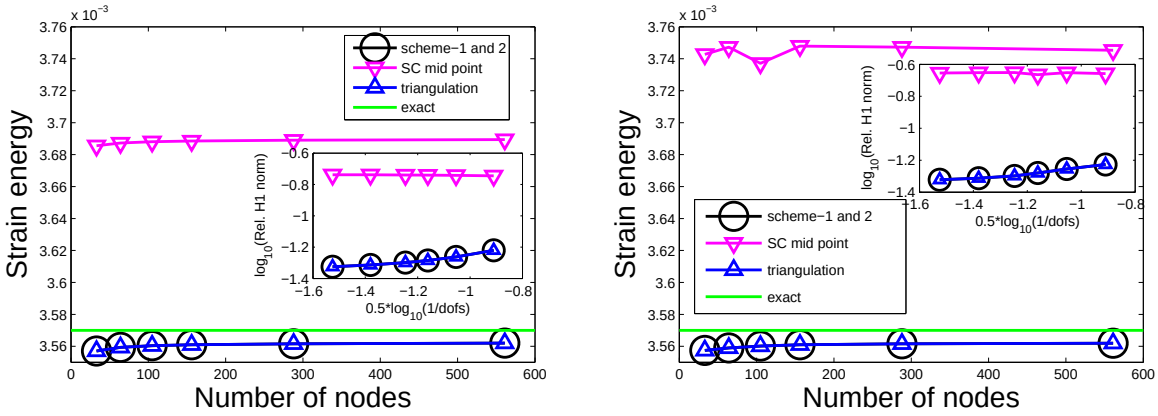

(a) (b)

Figure 3.6: Strain energy vs. number of nodes for meshes with 4-node quadrilateral elements under tensile loading. Rate of convergence of solution in H_1 is shown in the inset. (a) Structured mesh. (b) Unstructured mesh.

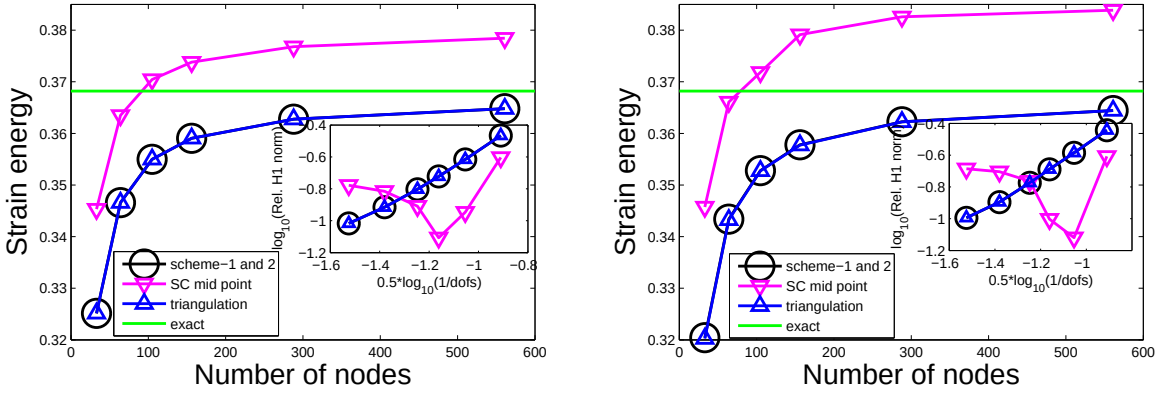

(a) (b)

Figure 3.7: Strain energy vs. number of nodes for meshes with 4-node quadrilateral elements under shear loading. Rate of convergence of solution in H_1 is shown in the inset. (a) Structured mesh. (b) Unstructured mesh.

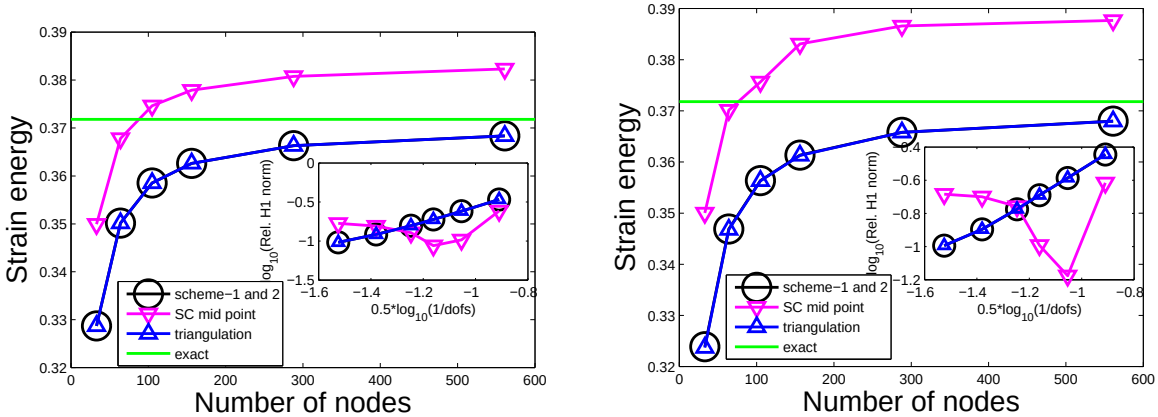

(a) (b)

Figure 3.8: Strain energy vs. number of nodes for meshes with 4-node quadrilateral elements under combined tension-shear loading. Rate of convergence of solution in H_1 is shown in the inset. (a) Structured mesh. (b) Unstructured mesh.

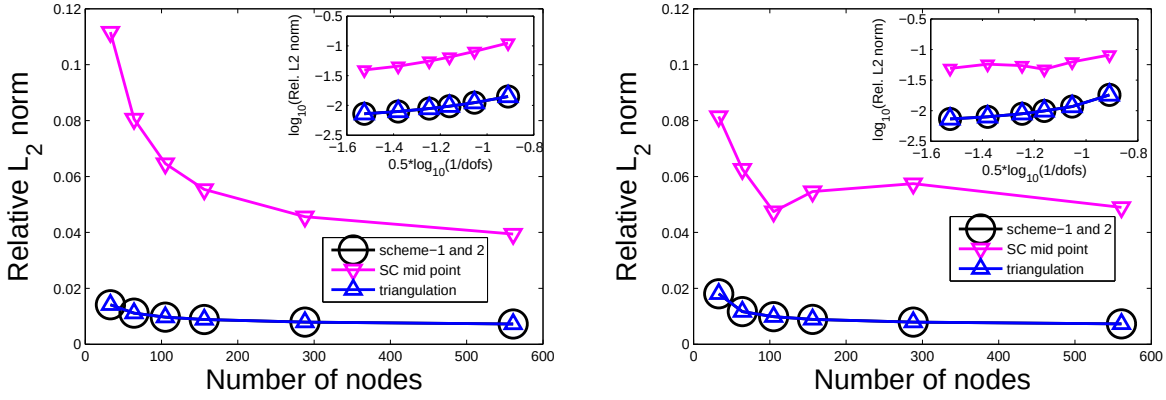

(a) (b)

Figure 3.9: Relative L_2 norm of displacement error vs. number of nodes for meshes with 4-node quadrilateral elements under tensile loading. Rate of convergence of solution in L_2 norm is shown in the inset. (a) Structured mesh. (b) Unstructured mesh.

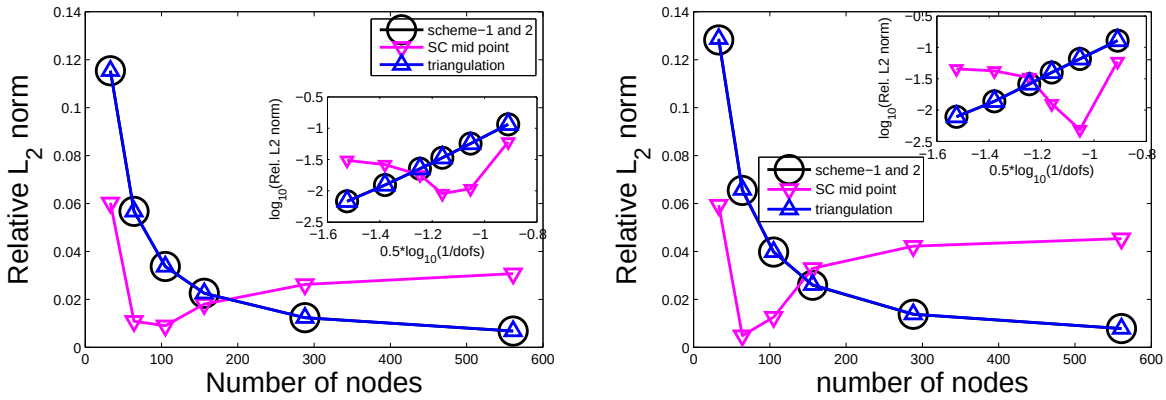

(a) (b)

Figure 3.10: Relative L_2 norm of displacement error vs. number of nodes for meshes with 4-node quadrilateral elements under shear loading. Rate of convergence of solution in L_2 norm is shown in the inset. (a) Structured mesh. (b) Unstructured mesh.

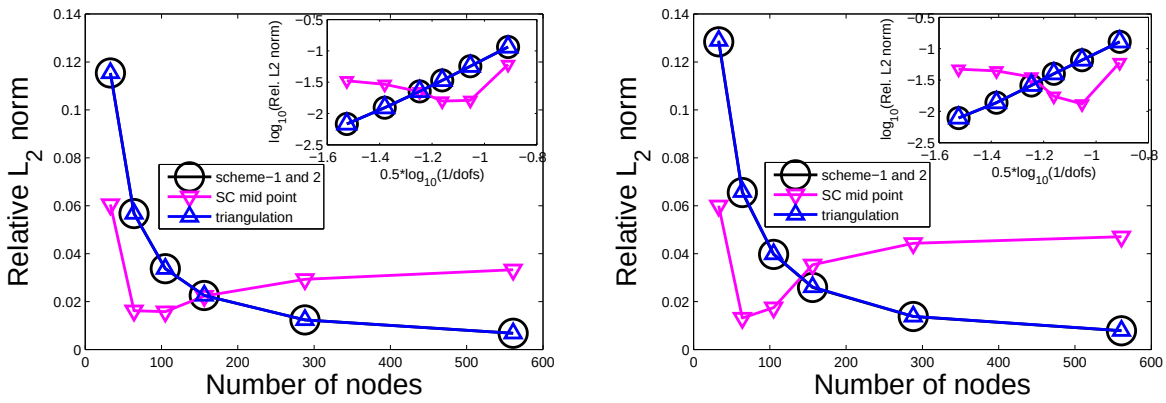

Figure 3.11: Relative L_2 norm of displacement error vs. number of nodes for meshes with 4-node quadrilateral elements under combined tension-shear loading. Rate of convergence of solution in L_2 norm is shown in the inset. (a) Structured mesh. (b) Unstructured mesh.

3.4 Analysis and Comparison of Results: Pentagons (n=5)

For pentagons there is no established optimal integration rule or isoparametric mapping known till date. Therefore we define the integration points in the unit-disk directly. Moreover the initial location of integration points is not important as we will be optimizing for the integration points. Since only 4 integration points were needed in the case of 4-node quadrilateral elements, intuitively we choose just 5 integration points for a 5-node pentagon. The scheme of placement of integration points on the unit-disk is shown in figure 2.4c. The coordinates of the integration points in Cartesian coordinate coordinate system are calculated from R and ϕ as

$$\xi_i = R\cos\left(\phi + \frac{2\pi}{5}(i-1)\right) \; ; \; \eta_i = R\sin\left(\phi + \frac{2\pi}{5}(i-1)\right) \tag{3.14}$$

for the i^{th} integration point, where $1 \leq i \leq 5$.

3.4.1 Scheme 1 applied to pentagons (n=5)

The triangulation method or the method proposed in Ref. [35] could be used to obtain the reference solution for a pentagonal element. We use the triangulation method, as discussed in section 2.4, with a large number of integration points to construct a reference solution. We use the integration rule given by Dunavant [42] with 79 integration points per triangle, where five symmetrically placed triangles represent the pentagon. This rule can be used to integrate polynomials of degree 20 exactly.

The error in Frobenius norm vs. R and ϕ is plotted in Figure 3.12. The values of R and ϕ corresponding to minimum error are given in table 3.2. We notice that the error in Frobenius norm in the stiffness matrix obtained using only 5 optimal integration points with SC mapping is very small when compared with the reference solution which uses 395 integration points in the pentagonal element.

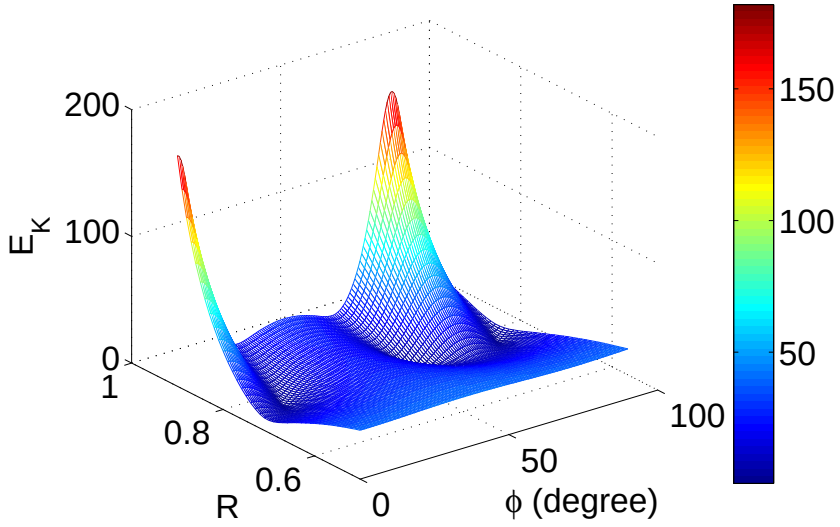

Figure 3.12: Error in Frobenius norm of u vs. coordinates (R, ϕ) of integration points on unit circle for 5-node pentagonal element.

Table 3.2: Optimal coordinate of integration points for 5-node pentagonal element

	Scheme 1	Scheme 2
Min. error	0.1506 % in E_K	5×10^{-9} in E_∞
R_{opt}	0.761	0.761
ϕ_{opt}	57.817^o	57.817^o

3.4.2 Scheme 2 applied to pentagons (n=5)

Figure 3.13 shows the finite element model with essential and natural boundary conditions used for optimization using scheme 2 for a pentagonal element. We use the same method to obtain the reference solution as used in scheme 1. The error in the infinity norm of the displacement as given by equation (3.10) vs. R and ϕ is plotted in figure 3.14. The values of R and ϕ corresponding to the minimum error are the coordinate of the optimal integration points. The optimal integration points obtained are given in table 3.2 and interestingly they are the same as those obtained by scheme 1 (down to three decimal places).

Since it is not possible to obtain a structured pentagonal mesh in a rectangular geometry, therefore only an unstructured mesh (figure 3.15) is used for comparison of

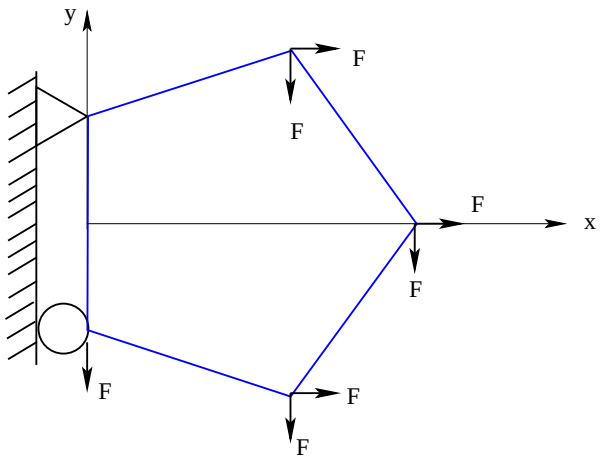

Figure 3.13: FE model with boundary conditions for scheme 2 based optimization for pentagonal element.

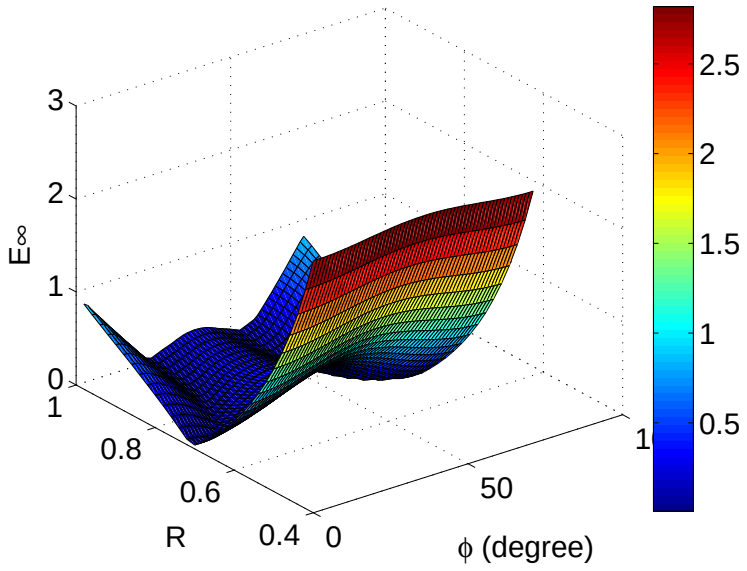

Figure 3.14: Error in infinity norm of u vs. coordinates (R, ϕ) of integration points on unit circle for 5-node pentagonal element.

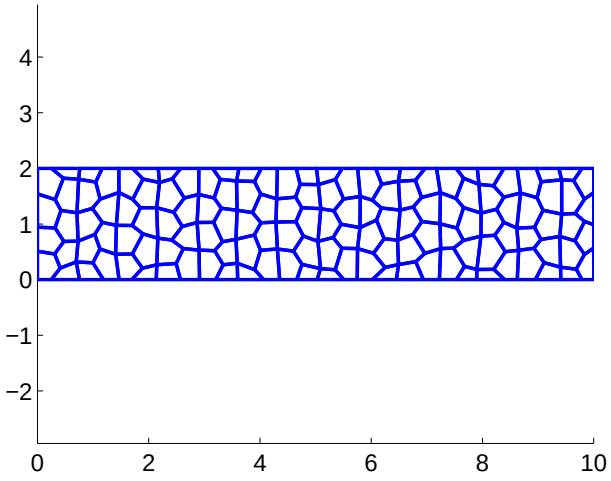

Figure 3.15: An unstructured mesh with pentagonal elements.

results. Convergence in strain energy versus number of nodes for pure tensile loading is shown in figure 3.16. There is an error of 16 % in strain energy when SC mid-point method is used with 208 nodes, whereas in case of the present method the error in strain energy is less than 0.2 % with same number of nodes. Figure 3.17 shows the convergence in strain energy versus number of nodes for pure shear loading. The present method with 5 optimal integration points needs around 400 nodes to achieve an error less than 1.5 % whereas the error in case of the SC mid-point method with same number of nodes is 5 %. Convergence rate for various cases are shown in inset in the corresponding figures. Convergence in strain energy versus number of nodes for combined loading is shown in figure 3.18.

Convergence in relative error in L_2 norm of displacement is plotted in figure 3.19 for tensile loading. In this case too the present method is much superior to SC mid-point method. In tensile loading case (figure 3.19), results show that there is an error of 0.8 % in relative L_2 norm in case of the present method with around 417 nodes. Whereas the SC mid-point method has an error of 4.5 % with the same number of nodes. For the case of shear loading (figure 3.20) the the error in L_2 norm with the present method is 1.3 % with around 417 nodes whereas the SC mid-point method gives an error of 4.7 % with same number of nodes. Convergence in relative error in L_2 norm of displacement

is plotted in figure 3.21 for combined loading.

In comparison to the triangulation scheme , to achieve the same accuracy as we have achieved using our scheme (i,e using only five integration points) the triangulation scheme need as much as sixty five integration points(i.e thirteen integration points per triangle).

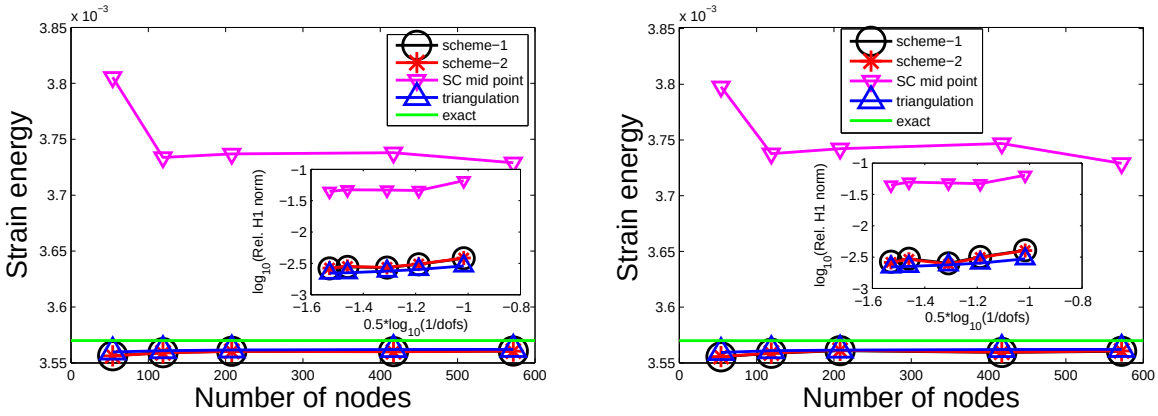

Figure 3.16: Strain energy vs. number of nodes for meshes with 5-node pentagonal elements under tensile loading. Rate of convergence of solution in H_1 is shown in the inset. (a) Structured mesh. (b) Unstructured mesh.

3.5 Analysis and Comparison of Results: Hexagons (n=6)

As pointed out in case of pentagons, there is no established optimal integration rule for $n > 4$. Therefore we define the integration points in the unit-disk as done in case of pentagons. Similarly, here also initial location of integration point is unimportant since we will be optimizing their coordinates. Intuitively we choose 6 integration points for a 6-node hexagon (n=6). The scheme for placement of integration points is shown in figure 2.5c. The coordinates of the integration points in Cartesian coordinate system are

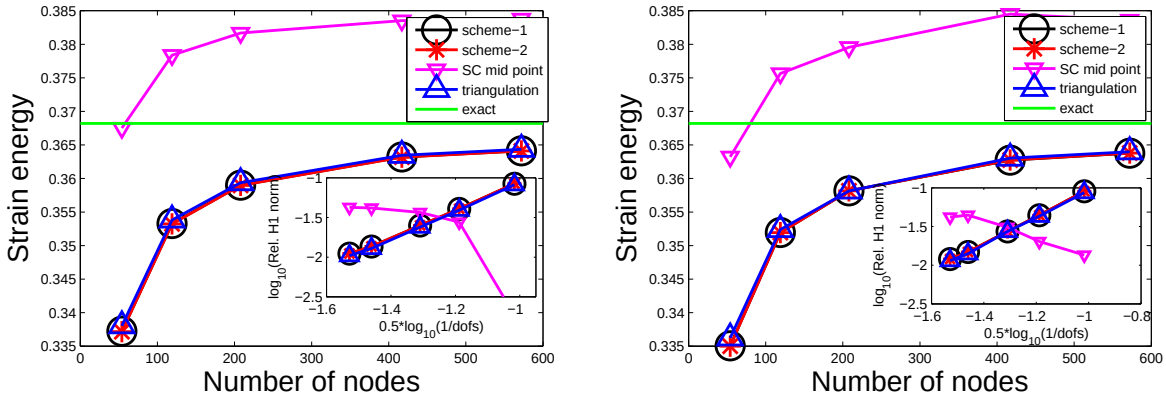

(a) (b)

Figure 3.17: Strain energy vs. number of nodes for meshes with 5-node pentagonal elements under shear loading. Rate of convergence of solution in H_1 is shown in the inset. (a) Structured mesh. (b) Unstructured mesh.

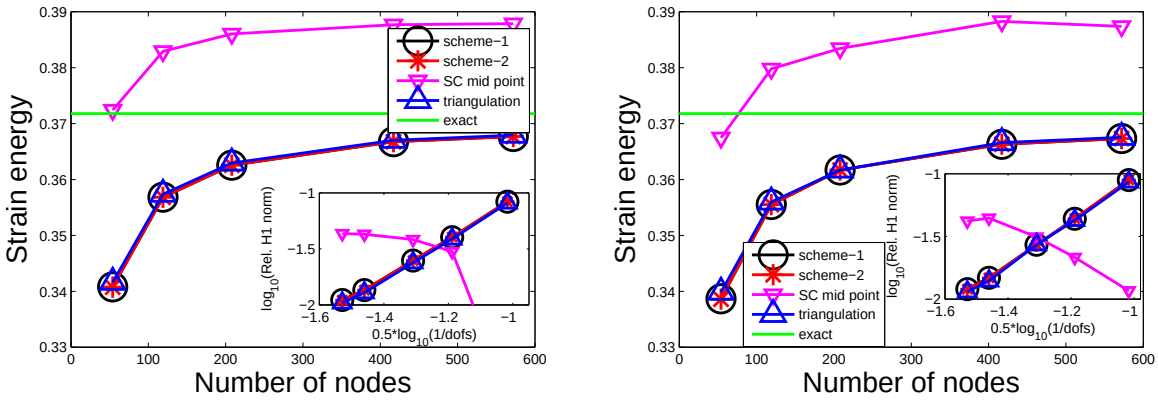

(a) (b)

Figure 3.18: Strain energy vs. number of nodes for meshes with 5-node pentagonal elements under combined tension-shear loading. Rate of convergence of solution in H_1 is shown in the inset. (a) Structured mesh. (b) Unstructured mesh.

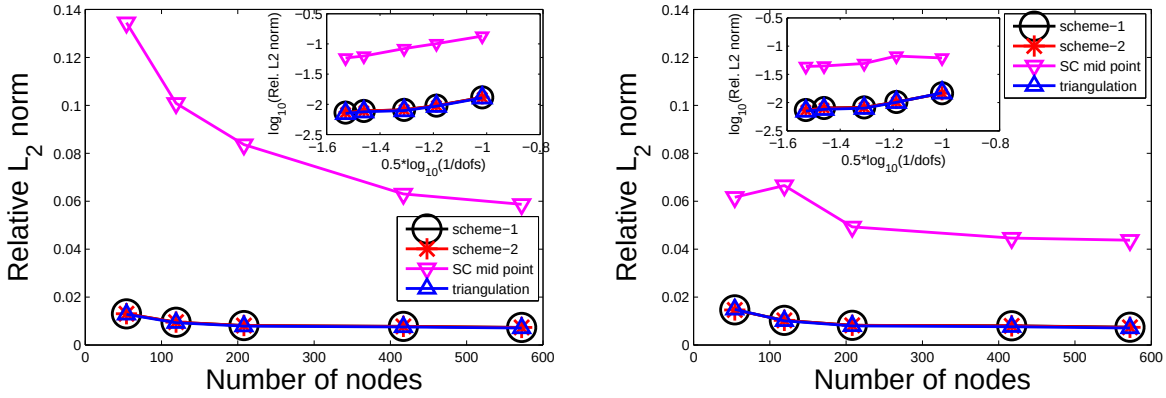

Figure 3.19: Relative L_2 norm of displacement error vs. number of nodes for meshes with 5-node pentagonal elements under tensile loading. Rate of convergence of solution in L_2 norm is shown in the inset. (a) Structured mesh. (b) Unstructured mesh.

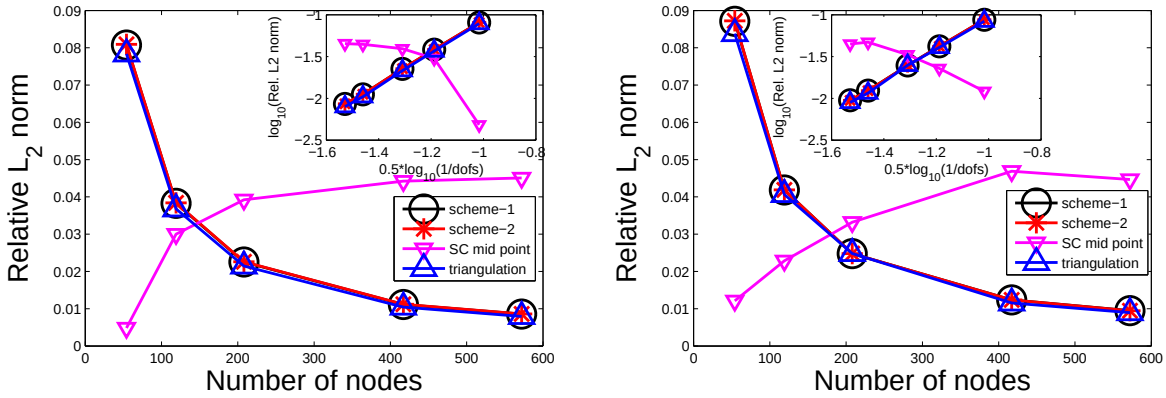

Figure 3.20: Relative L_2 norm of displacement error vs. number of nodes for meshes with 5-node pentagonal elements under shear loading. Rate of convergence of solution in L_2 norm is shown in the inset. (a) Structured mesh. (b) Unstructured mesh.

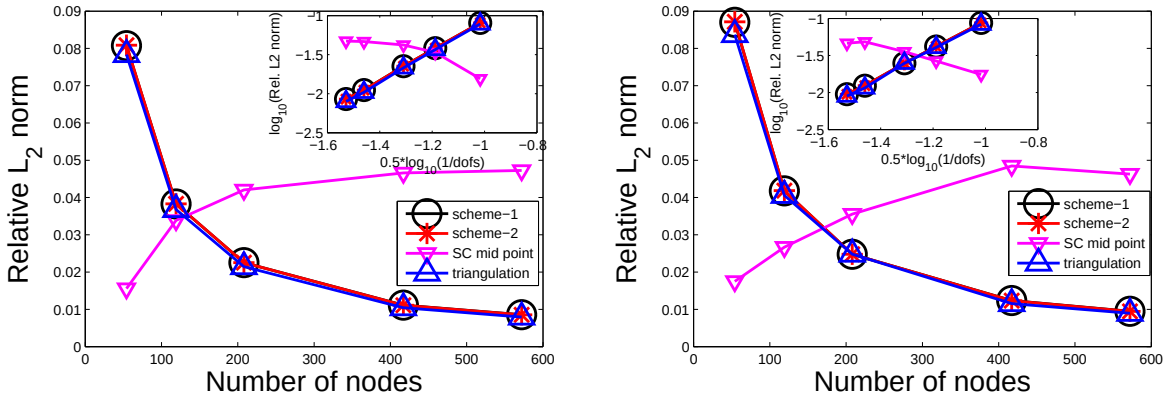

Figure 3.21: Relative L_2 norm of displacement error vs. number of nodes for meshes with 5-node pentagonal elements under combined tension-shear loading. Rate of convergence of solution in L_2 norm is shown in the inset. (a) Structured mesh. (b) Unstructured mesh.

calculated as

$$\xi_i = R\cos\left(\phi + \frac{2\pi}{6}(i-1)\right) \; ; \; \eta_i = R\sin\left(\phi + \frac{2\pi}{6}(i-1)\right) \tag{3.15}$$

for the i^{th} integration point, where $1 \leq i \leq 6$.

3.5.1 Scheme 1 applied to hexagons (n=6)

The triangulation method or the method proposed in Ref. [35] could be used to obtain the reference solution for a hexagonal element. We use the triangulation method, as discussed in section 2.4, with a large number of integration points to construct a reference solution. Here we use integration rule given by Dunavant [42] with 79 integration points per triangle as done in the case of pentagons.

The error in the Frobenius norm vs. R and ϕ is plotted in Figure 3.22. The values of R and ϕ corresponding to the minimum error are given in table 3.3. We notice that the error in the Frobenius norm of stiffness matrix obtained using just 6 optimal integration points with SC mapping is very small when compared with the reference solution which uses 474 integration points element.

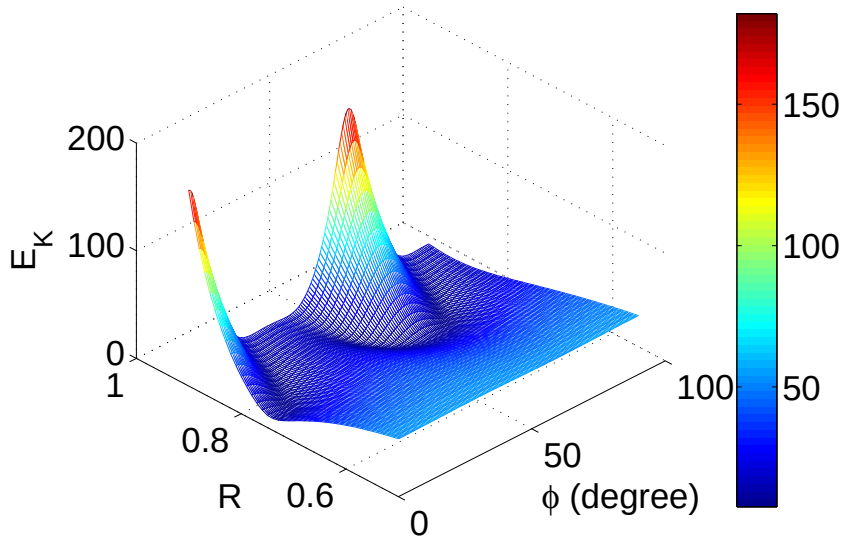

Figure 3.22: Error in Frobenius norm of u vs. coordinates (R, ϕ) of integration points on unit circle for 6-node hexagonal element.

Table 3.3: Optimal coordinate of integration points for 6-node hexagonal element.

	Scheme 1 (fig. 2.5b)	Scheme 2
Min. error	7.6089 % in E_K	2×10^{-7} in E_∞
R_{opt}	0.788	0.797
ϕ_{opt}	46.719^o	46.811^o

3.5.2 Scheme 2 applied to hexagons (n=6)

Figure 3.23 shows the finite element model with essential and natural boundary conditions used for optimization using scheme 2 for a hexagonal element. We use the same method for getting reference solution as used in scheme 1. The error in the infinity norm of displacement as given by equation (3.10) vs. R and ϕ is plotted in figure 3.24. The values of R and ϕ corresponding to minimum error are given in table 3.3.

Figure 3.25 shows a structured mesh and an unstructured mesh with 6-node hexagonal elements. Convergence in strain energy versus the number of nodes for structured and unstructured mesh under pure tension are shown in figures 3.26a and 3.26b, respectively.It is clear from the figures that strain energy varies by less than 0.25 % between mesh 1 and mesh 2 for the present method with 6 optimal integration points. On the

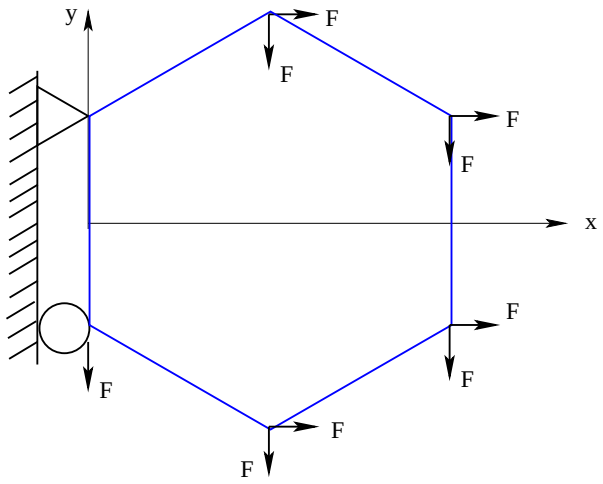

Figure 3.23: FE model with boundary conditions for scheme 2 based optimization for hexagonal element.

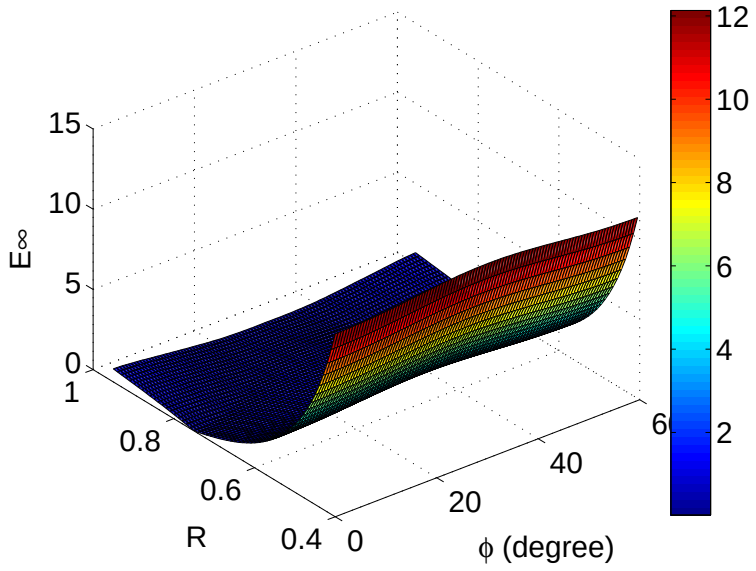

Figure 3.24: Error in infinity norm of u vs. coordinates (R, ϕ) of integration points on unit circle for 6-node hexagonal element.

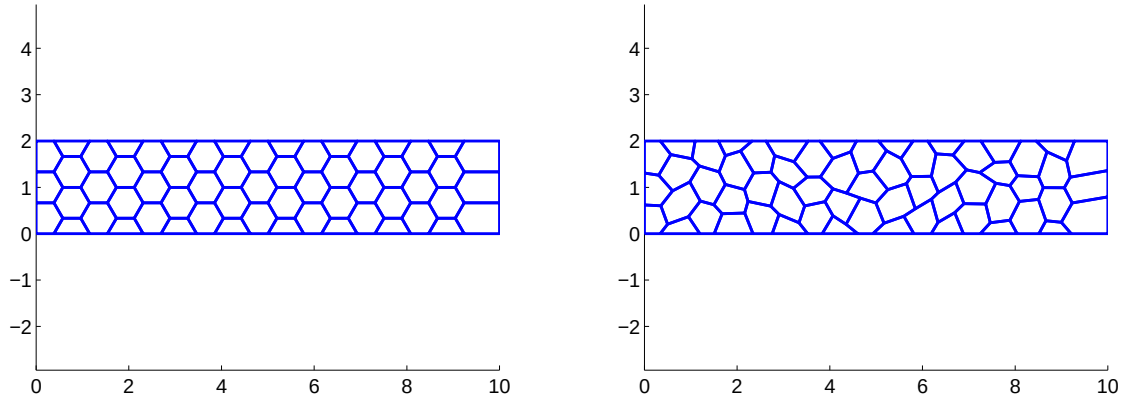

Figure 3.25: (a) Structured mesh and (b) unstructured mesh with hexagonal elements.

other hand the SC mid-point method with the same number of integration points does not converge to the exact value even for 450 nodes for which the error is still 9.8 %. Figure 3.27a shows the convegence curves under shear loading case for hexagonal structured mesh. It converges at 208 nodes with an error of less than 1.5 %. Whereas in the case of SC mid-point method there is a saturation in strain energy with about 450 nodes for an error of 1.5 % but it never converges. Similar observations are made for the unstructured hexagonal mesh too (3.27b). The solution seems to be slightly diverging in case of the present method for tensile loading case. However the error in energy norm is $\leq 1\%$ even for the largest value of error. Convergence in strain energy versus the number of nodes for structured and unstructured mesh under combined loading are shown in figures 3.28a and 3.28b, respectively.

Convergence in relative error in L_2 norm of displacement is plotted in from figure 3.29 to 3.31. Here also the convergence curves show similar trends as observed in case of convergence in strain energy. It is also seen that the two schemes give almost similar results due to the fact that the difference in the coordinates of integration points is small.

In comparison to the triangulation scheme, to achieve the same accuracy as we have achieved using our scheme (i,e using only six integration points) the triangulation scheme

need as much as seventy eight integration points(i.e thirteen integration points per triangle). And for Generalized Gaussian Quadrature[35] it is giving as good result as our scheme with six integration points or higher for hexagonal element. But Generalized Gaussian Quadrature is giving poor result if we use lesser number of integration points.

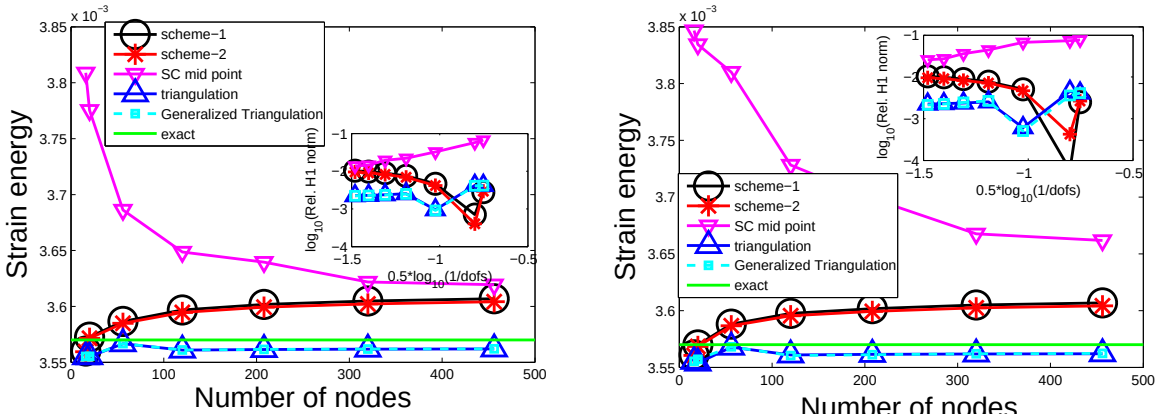

Figure 3.26: Strain energy vs. number of nodes for meshes with 6-node hexagonal elements under tensile loading. Rate of convergence of solution in H_1 is shown in the inset. (a) Structured mesh. (b) Unstructured mesh.

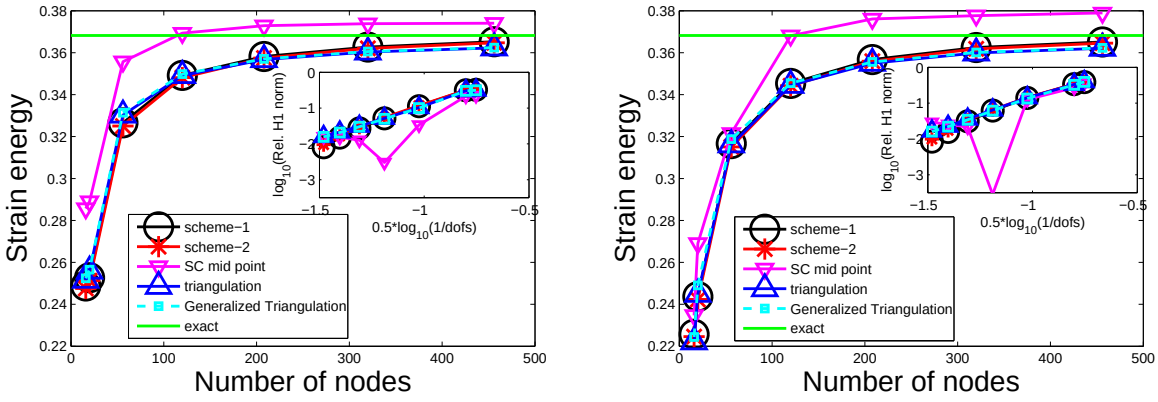

(a) (b)

Figure 3.27: Strain energy vs. number of nodes for meshes with 6-node hexagonal elements under shear loading. Rate of convergence of solution in H_1 is shown in the inset. (a) Structured mesh. (b) Unstructured mesh.

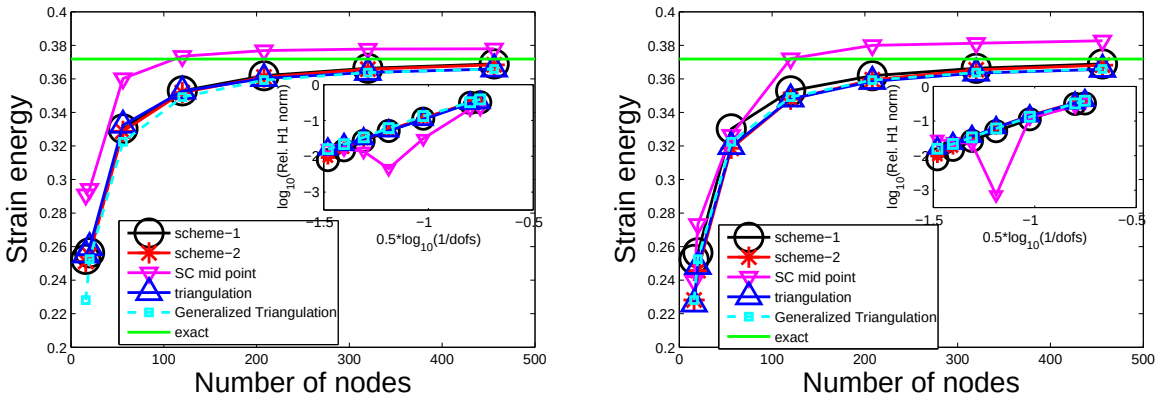

(a) (b)

Figure 3.28: Strain energy vs. number of nodes for meshes with 6-node hexagonal elements under combined tension-shear loading. Rate of convergence of solution in H_1 is shown in the inset. (a) Structured mesh. (b) Unstructured mesh.

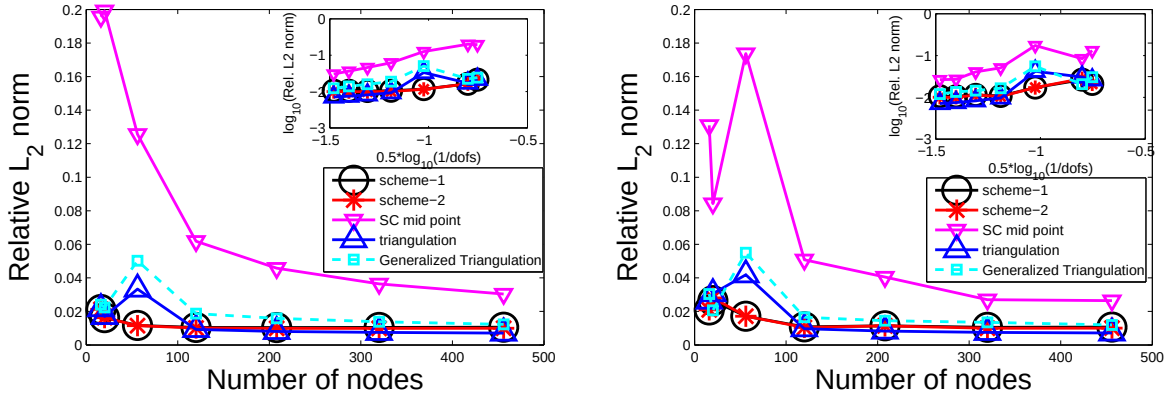

(a) (b)

Figure 3.29: Relative L_2 norm of displacement error vs. number of nodes for meshes with 6-node hexatagonal elements under tensile loading. Rate of convergence of solution in L_2 norm is shown in the inset. (a) Structured mesh. (b) Unstructured mesh.

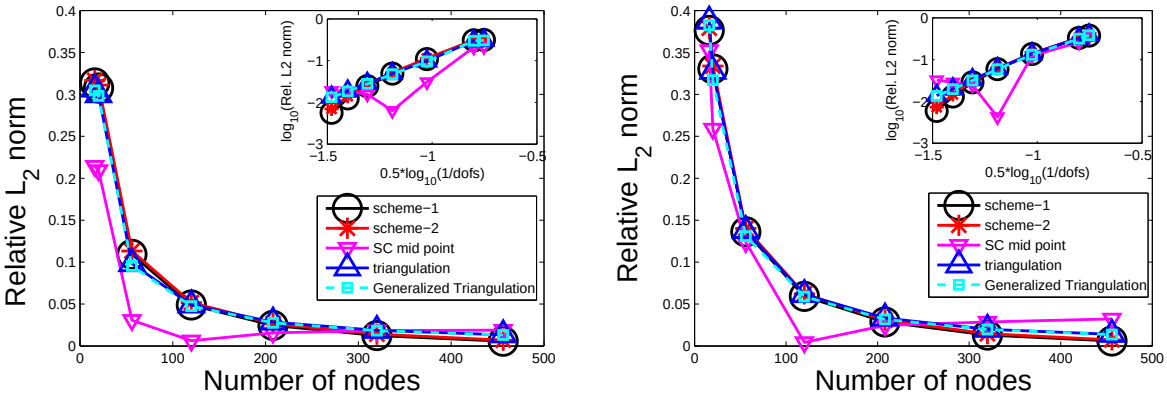

(a) (b)

Figure 3.30: Relative L_2 norm of displacement error vs. number of nodes for meshes with 6-node hexagonal elements under shear loading. Rate of convergence of solution in L_2 norm is shown in the inset. (a) Structured mesh. (b) Unstructured mesh.

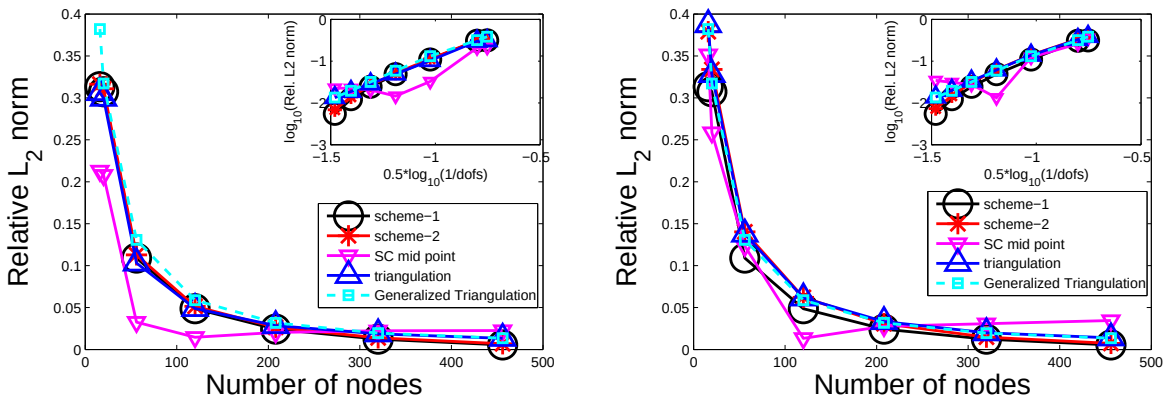

Figure 3.31: Relative L_2 norm of displacement error vs. number of nodes for meshes with 6-node hexatagonal elements under combined tension-shear loading. Rate of convergence of solution in L_2 norm is shown in the inset. (a) Structured mesh. (b) Unstructured mesh.

Chapter 4

Polygonal Finite Element Method for Polycrystalline Material

4.1 Problem Defination

Up to previous chapter the material has been considered as an isotropic and homogenious material. But most of the structural material is polycrystaline in nature where the grain size and it's orientatin varies depending on the heat treatment during the processing of the material. Figure 4.1 shows a typical aluminium alloy microstructure.

We convert this microstructure image of the material to a finite element mesh (figure 4.2).

Since it is not possible to get the microstructure image of whole structure we use a representative volum element(RVE) (figure 4.3) and fill the whole structure using that representative volume.

4.2 FEM formulation for polycrystal material

For polycrystalline material the Finite Element formulation is same as discussed in section(2.1) with the expression for stiffness matrix given by

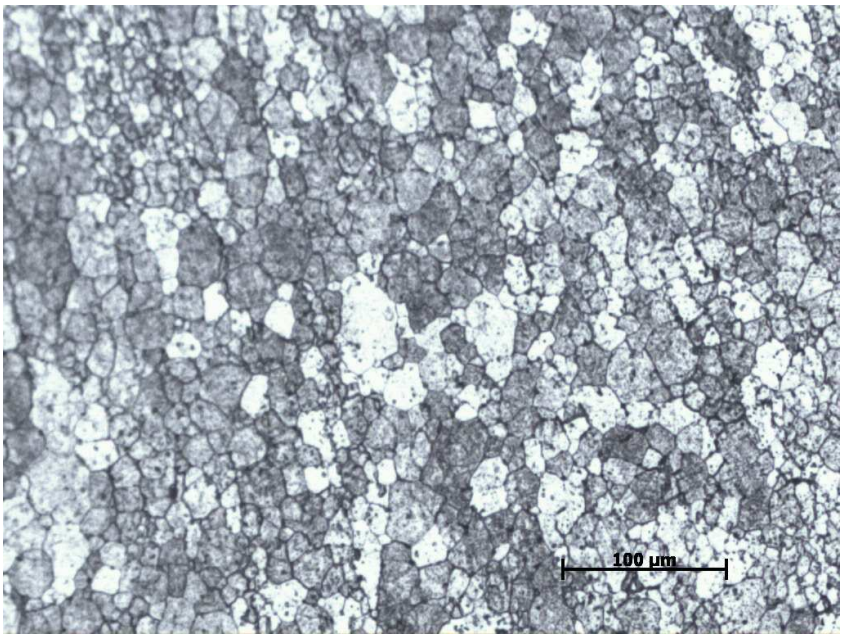

Figure 4.1: Typical microstructure image of aluminium alloy 2219-T87 (image courtesy: Material Research Center,IISc).

$$\mathbf{K} = \int_{\Omega^h} \mathbf{B^T D B} d\Omega \tag{4.1}$$

But in this case **D** matrix varies from element to element based on the orientation of that polycrystal grain with respect to the global co-ordinate. And is given by

$$\mathbf{D} = \mathbf{T^T D_h T} \tag{4.2}$$

where **T** is the transformation matrix written as

$$\mathbf{T} = \begin{bmatrix} Cos^2(\theta) & Sin^2(\theta) & 2Cos(\theta)Sin(\theta) \\ Sin^2(\theta) & Cos^2(\theta) & -2Cos(\theta)Sin(\theta) \\ -Cos(\theta)Sin(\theta) & Cos(\theta)Sin(\theta) & Cos^2(\theta) - Sin^2(\theta) \end{bmatrix} \tag{4.3}$$

where θ is the angle between local material axis and the global axis as shown in figure(4.4) D_h is constitutive matrix in 2D. For plane stress

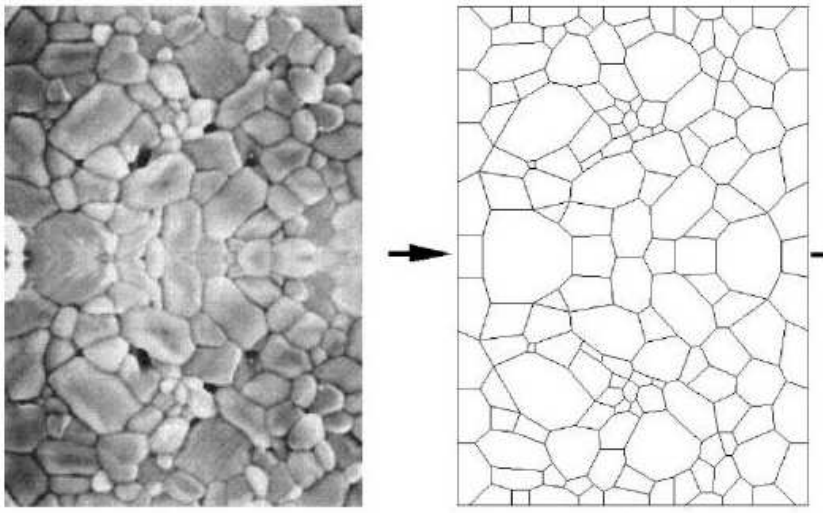

Figure 4.2: Typical example for conversion of microstructure image to Finite element mesh.

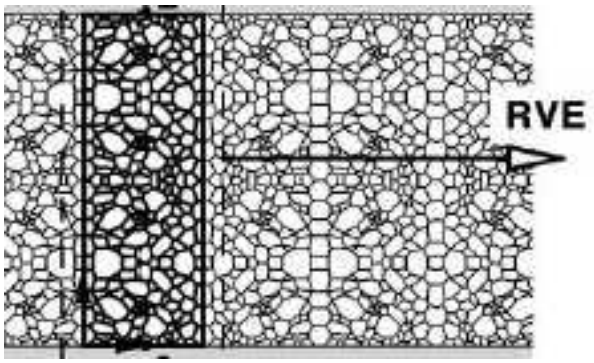

Figure 4.3: Representative volume element.

$$\mathbf{D_h} = \frac{E}{(1+v)(1-2v)} \begin{bmatrix} (1-v) & v & 0 \\ v & (1-v) & 0 \\ 0 & 0 & \frac{1-2v}{2} \end{bmatrix} \tag{4.4}$$

and for plane strain D_h is

$$\mathbf{D_h} = \frac{E}{(1+v)(1-2v)} \begin{bmatrix} (1-v) & v & 0 \\ v & (1-v) & 0 \\ 0 & 0 & \frac{1-2v}{2} \end{bmatrix} \tag{4.5}$$

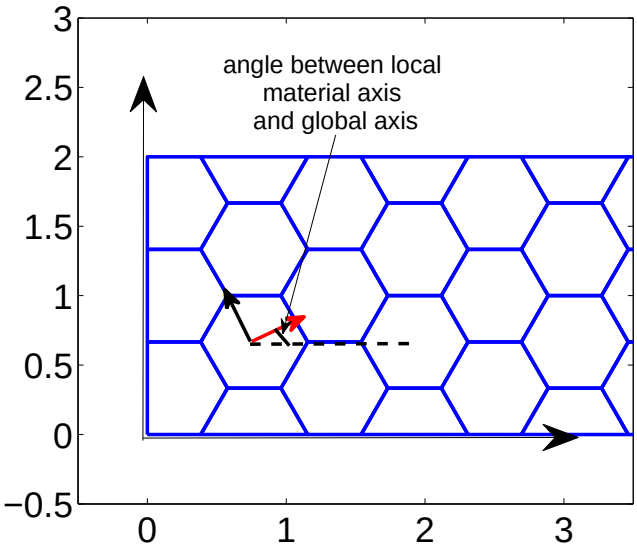

Figure 4.4: Typical polycrystalline element to show the angle(θ) between local material axis and global axis.

4.3 Integration Scheme

Since we use numerical integration scheme to get the individual member of the stiffness matrix, so proper placing of the integration points are crucial to incorporate any types of nonhomogenity in the element domain. Here we are using the same integration scheme as discussed in section 3 with some modification. Figure 4.5a, figure 4.5b and figure 4.5c shows the placing of optimised integration points for quadrilaterla, pentagonal and hexagonal element as per section 3.

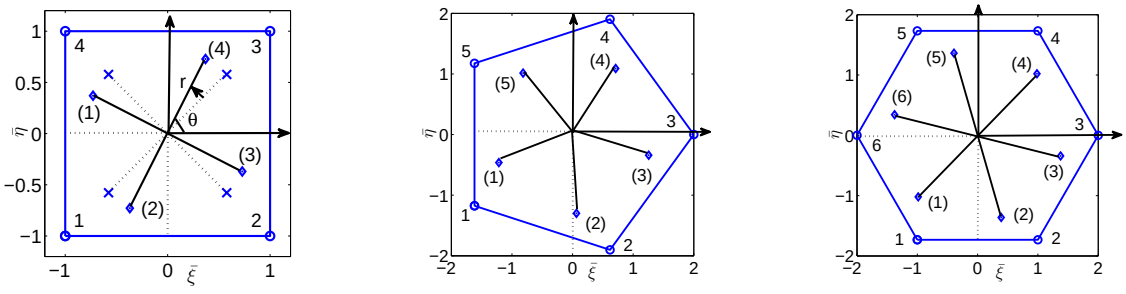

(a) (b) (c)

Figure 4.5: Optimum integration points. (a) Quadrilateral element. (b) Pentagonal element. (c) Hexagonal element.

in excess to these optimised integration points few extra integration points near the element boundary have been used to incorporate the smooth variation of material property across the element boundary wirh respect to the globa co-ordinate system. Figure(4.6) shows the placing of these integration points for quadrilateral, pentagonal, hexagonal element respectively.

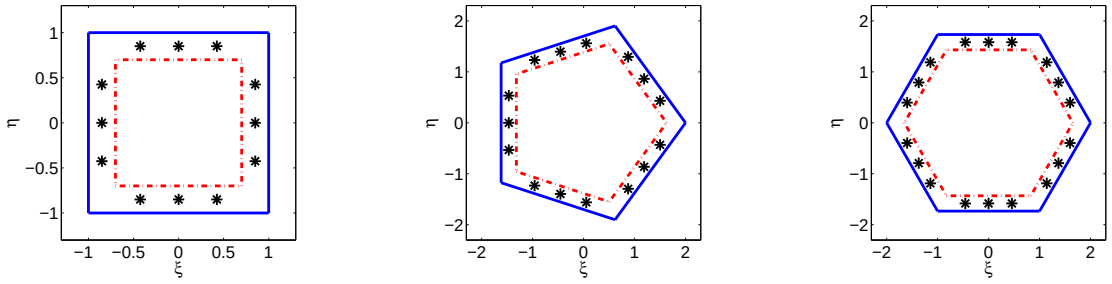

Figure 4.6: Extra integration points. (a) Quadrilateral element. (b) Pentagonal element. (c) Hexagonal element.

4.4 Numerical results and Discussion

Since material property is varying from element to element we can't get the solution of displacement of entire beam in analytic form. So strain energy has been compared for different types of meshing using different element. Table(4.1) shows strain energy of the same beam under same loading and support condition but modelling of the material is different. Column 2 represents the strain energy with material being modelled as polycrystalline in nature and in column 3 the material has been modelled as homogenious throughout the beam.

Figure 4.7 to figure 4.12 shows the element wise principle material axis and displacement shape comparison between two types of material modelling, one polycrystaline material where material property is varying from element to element and another is considering the material as homogenious through out the beam.

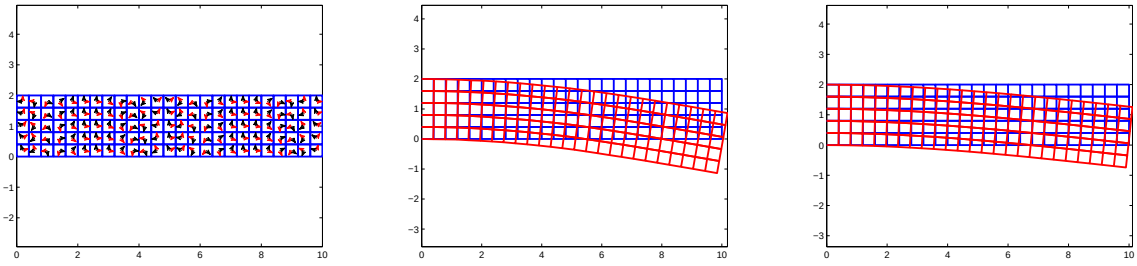

(a) (b) (c)

Figure 4.7: Polycrystalline meshing using quadrilateral structured mesh. (a) Element wise principle material axis. (b) Displacement shape(100 times magnified) (c) Displacement shape for same beam with no material axis rotation(100 times magnified).

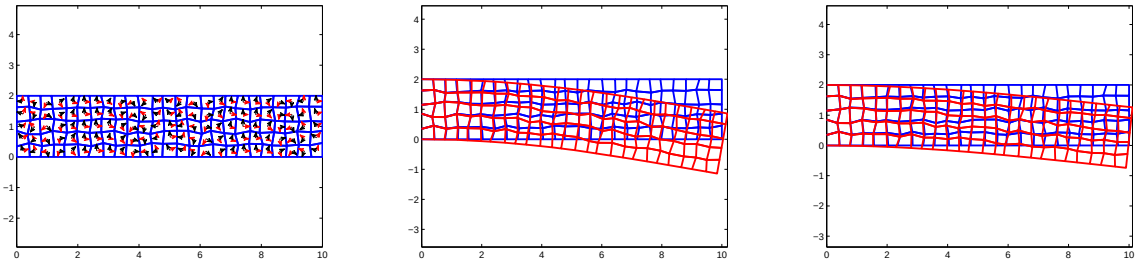

(a) (b) (c)

Figure 4.8: Polycrystalline meshing using quadrilateral unstructured mesh. (a) Element wise principle material axis. (b) Dsplacement shape(magnified). (c) Displacement shape for same beam with no material axis rotation(100 times magnified)

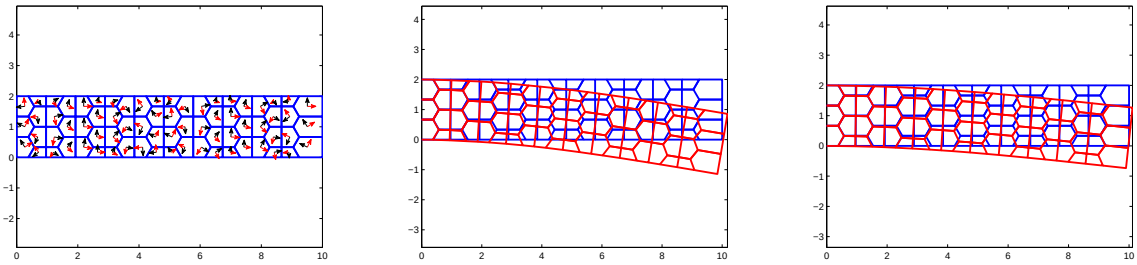

(a) (b) (c)

Figure 4.9: Polycrystalline meshing using pentagonal structured mesh. (a) Element wise principle material axis. (b) Dsplacement shape(magnified). (c) Displacement shape for same beam with no material axis rotation(100 times magnified).

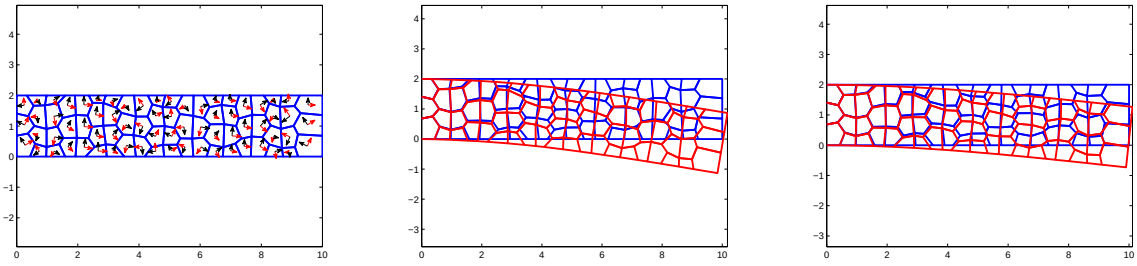

(a) (b) (c)

Figure 4.10: Polycrystalline meshing using pentagonal unstructured mesh. (a) Element wise principle material axis. (b) Dsplacement shape(magnified). (c) Displacement shape for same beam with no material axis rotation(100 times magnified).

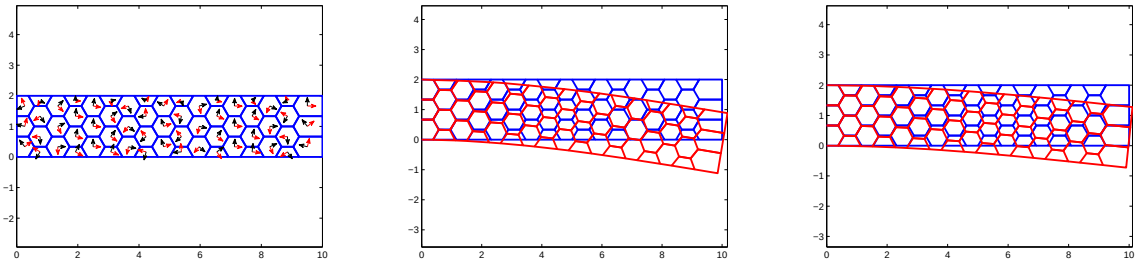

(a) (b) (c)

Figure 4.11: Polycrystalline meshing using hexagonal structured mesh. (a) Element wise principle material axis. (b) Dsplacement shape(magnified). (c) Displacement shape for same beam with no material axis rotation(100 times magnified).

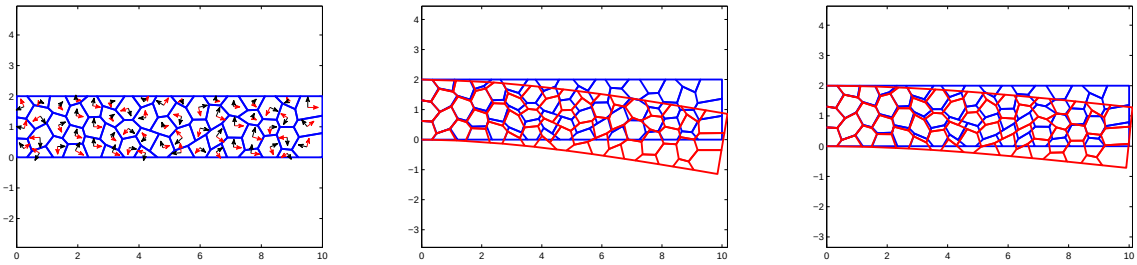

(a) (b) (c)

Figure 4.12: Polycrystalline meshing using hexagonal unstructured mesh. (a) Element wise principle material axis. (b) Dsplacement shape(magnified). (c) Displacement shape for same beam with no material axis rotation(100 times magnified).

Table 4.1: Strain Energy Of the Beam

Meshing Type	Polycrystalline Material	Homogeneous Material
Structured Quadrilateral	0.575679061435	0.362624510505
Unstructured Quadrilateral	0.578080920760	0.361353410955
Structured Pentagonal	0.577148899855	0.356837210113
Unstructured Pentagonal	0.571157734828	0.355529565734
Structured Hexagonal	0.566037973585	0.352860719057
Unstructured Hexagonal	0.579808616236	0.352860719057

From the above results of displacement shapes it is clear that if we model a polycrystaline material as an isotropic homogenious material then there will be significant error in the prediction of displacement and consequentially other structural parameter.

Chapter 5

Extended Finite Element Method: Formulation

5.1 Governing Equations and Weak Form

The governing equilibrium equations for a 2D static elasticity problem defined in the domain Ω bounded by Γ and $\Gamma = \Gamma_u \cup \Gamma_t \cup \Gamma_c$ (fig. 5.1), can be expressed as

$$\nabla_s^{\mathrm{T}} \boldsymbol{\sigma} + \mathbf{b} = \mathbf{0} \quad \text{in } \Omega \tag{5.1}$$

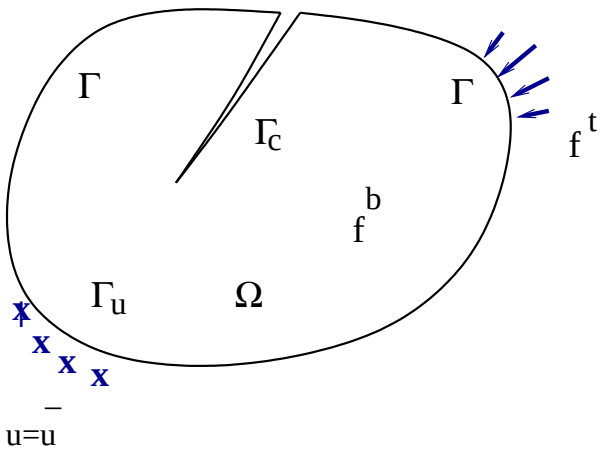

Figure 5.1: A body in a state of elastostatic equilibrium.

where **0** is a null vector, $\boldsymbol{\sigma}$ is the stress tensor and b is the vector of external forces. The following are the prescribed boundary conditions

$$\mathbf{u} = \overline{\mathbf{u}} \ in \ \Gamma_u \tag{5.2a}$$

$$\mathbf{n}^T\boldsymbol{\sigma} = \overline{\mathbf{t}} \ on \ \Gamma_t \tag{5.2b}$$

$$\mathbf{n}^T\boldsymbol{\sigma} = \mathbf{0} \ on \ \Gamma_c \tag{5.2c}$$

where $\overline{\mathbf{u}} = (\overline{u}_x, \overline{u}_y)^T$ is the prescribed displacement vector on the essential boundary Γ_u; $\mathbf{t} = (\overline{t}_x, \overline{t}_y)^T$ is the prescribed traction vector on the natural boundary Γ_t and Γ_c is the traction free boundary condition at crack all faces; $\mathbf{n}$ is the unit outward normal vector. The discrete version of the weak form for this problem are obtained using Galerkin approach as

$$\int_\Omega (\bigtriangledown_s \delta\mathbf{u})^T \mathbb{D} (\bigtriangledown_s \mathbf{u}) d\Omega - \int_\Gamma (\delta\mathbf{u}^T)\mathbf{b} d\Omega - \int_\Gamma (\delta\mathbf{u})^T \overline{\mathbf{t}} d\Gamma = 0 \tag{5.3}$$

where $\mathbf{u}$ and $\delta\mathbf{u}$ are the test functions that belong to admissible functions from Sobolev space and $\mathbb{D}$ is the constitutive matrix. The extended finite element method uses the following trial function $\mathbf{u}_h(\mathbf{x})$ and the test function $\delta\mathbf{u}_h(\mathbf{x})$:

$$\mathbf{u}_h(\mathbf{x}) = \sum_{i=1}^{N_P} \mathbf{N}_i(\mathbf{X})\mathbf{u}_i + \sum_{j=1}^{m} \mathbf{N}_k(\mathbf{X})\psi(\mathbf{X})\mathbf{a}_k \tag{5.4a}$$

$$\delta\mathbf{u}_h(\mathbf{x}) = \sum_{i=1}^{N_P} \mathbf{N}_i(\mathbf{X})\delta\mathbf{u}_i + \sum_{j=1}^{m} \mathbf{N}_k(\mathbf{X})\psi(\mathbf{X})\delta\mathbf{a}_k + \sum_{j=1}^{m} \mathbf{N}_k(\mathbf{X})\delta\psi(\mathbf{X})\mathbf{a}_k \tag{5.4b}$$

where N_P is the total number of nodes in the mesh, m is the number of enriched nodes, $\mathbf{a}_k$ is the set of degrees of freedom added to the standard finite element modal degrees of freedom and $\psi(\mathbf{X})$ is the discontinuous enrichment function. By substituting the approximations $\mathbf{u}^h$ and $\delta\mathbf{u}^h$ into the weak form and invoking the arbitrariness of virtual nodal displacements, equation (5.3) yields the standard discretized algebraic system of equations:

$$\mathbf{K}\mathbf{u} = \mathbf{f} \tag{5.5}$$

with the stiffness matrix given by

$$\mathbf{K_{ij}^{e}} = \begin{bmatrix} \mathbf{K_{ij}^{uu}} & \mathbf{K_{ij}^{ua}} & \mathbf{K_{ij}^{uc}} \\ \mathbf{K_{ij}^{au}} & \mathbf{K_{ij}^{aa}} & \mathbf{K_{ij}^{ac}} \\ \mathbf{K_{ij}^{cu}} & \mathbf{K_{ij}^{ca}} & \mathbf{K_{ij}^{cc}} \end{bmatrix} \tag{5.6}$$

and the load vector by

$$\mathbf{f_i} = \begin{bmatrix} \mathbf{f_i^u} & \mathbf{f_i^a} & \mathbf{f_i^{c1}} & \mathbf{f_i^{c2}} & \mathbf{f_i^{c3}} & \mathbf{f_i^{c4}} \end{bmatrix}^T \tag{5.7}$$

$\mathbf{u}$ is a vector of nodal parameters and given by

$$\mathbf{u^h} = \begin{bmatrix} \mathbf{u} & \mathbf{a} & \mathbf{c1} & \mathbf{c2} & \mathbf{c3} & \mathbf{c4} \end{bmatrix}^T \tag{5.8}$$

5.2 Crack Modeling Using Discontinuous Enrichment

The main idea in Partition of Unity Methods is to extend the approximation basis by a set of enrichment functions that are chosen based on the local behavior of the problem. For the case of linear elastic fracture mechanics, two sets of functions are used: a Heaviside jump function to capture the jump across the crack faces and asymptotic branch functions that span the 2D asymptotic crack tip fields. The enriched approximation for fracture mechanics problems takes the form [4]:

$$\mathbf{u^h}(\mathbf{x}) = \sum_{i \in I} N_i(\mathbf{x})\, \mathbf{u_i} + \sum_{j \in J} N_j(\mathbf{x})\, H(\mathbf{x})\, \mathbf{a_j} + \sum_{j \in K} N_j(\mathbf{x}) \sum_{\alpha=1}^{4} \psi_\alpha(\mathbf{x})\, \mathbf{b_{k\alpha}} \tag{5.9}$$

$N_i(x)$ is the polygonal basis function of node i. Where $\mathbf{a_j}$ and $\mathbf{b_{k\alpha}}$ are enrichment nodal degrees of freedom corresponding to the Heaviside function H and the near-tip functions ψ_α, respectively. Signed distance function for Heaviside function H is given by

$$H(\xi) = \begin{cases} 1 & \forall \xi > 0 \\ -1 & \forall \xi < 0 \end{cases} \tag{5.10}$$

where ξ is the signed distance from a point $\mathbf{x}$ to an interface Γ. The near tip enrichment functions ψ_α are defined in terms of local coordinates (r, θ) and given as

$$\psi_\alpha(r,\theta) = \left\{ \sqrt{r}\sin\frac{\theta}{2},\quad \sqrt{r}\cos\frac{\theta}{2},\quad \sqrt{r}\sin\theta\sin\frac{\theta}{2},\quad \sqrt{r}\sin\theta\cos\frac{\theta}{2} \right\} \tag{5.11}$$

Approximation (5.9) is not an interpolation as nodal parameter $\mathbf{u_i}$ is not the real displacement value at node i. To overcome this shortcoming a shifting procedure is implemented. That is the Heaviside function and near-tip functions are shifted around the node of interest [46]. Figure(5.2) shows the Heviside enriched nodes and crack tip enrich nodes for a typical beam with crack.

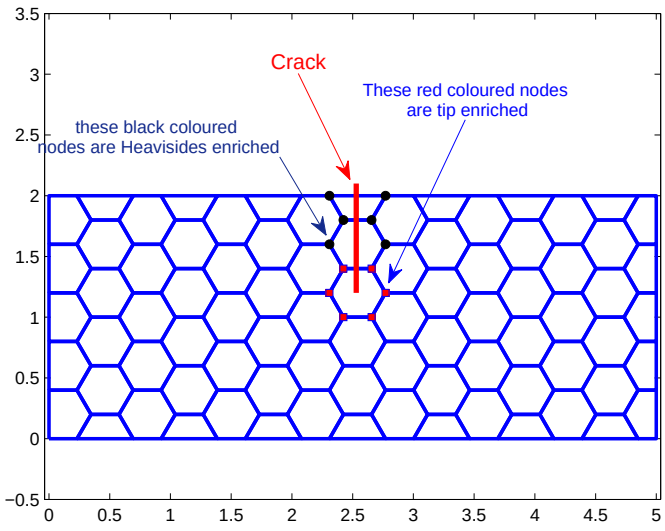

Figure 5.2: Heviside enrichment and tip enrichment for a typical beam problem with crack.

5.3 Numerical Integration

Numerical integration of the weak form of the governing equation presents a major challenge in XFEM. This is due to the presence of the Heaviside enrichment function which is discontinuous across the crack. For integrals involving discontinuous functions, we divide the element into sub-elements. And hence the integrands become continuous on

each sub-elements. For elements intersected by crack, we modify the element quadrature routines to accurately assemble the contribution to the weak form on both sides of the discontinuity. The discrete weak form is usually constructed with a loop over all elements, as the domain is approximated by

$$\Omega = \sum_{e} \Omega_e$$

where Ω_e is the element subdomain. For elements cut by a crack, we define the element sub-domain to be a sum of a set of sub-polygons (Ω_s) whose boundaries align with the crack geometry

$$\Omega_e = \sum_{s} \Omega_s$$

We divide the elements into triangles. The subpolygons are only necessary for integration purposes as no additional degrees of freedom are associated with their construction. In the integration of the weak form, an additional loop over sub-polygons is incorporated for the elements that are divided into sub-polygons.

In case of elements with tip enrichments this subdivision is crucial to capture the effect of high stress gradients in the vicinity of the crack. We generally refer to intersected elements as well as blending elements as enriched elements. We use the following two different numerical integration scheme based on the element type.

1. Integration on unenriched elements is performed by two-level mapping scheme with optimal integration points for integration as described in chapter 3. An arbitrary polygon is first mapped to a reference polygon using isoparametric mapping. The reference polygon is then mapped to unit circle. The integration is done over this unit disc. We use 4, 5 and 6 optimal integration points for 4-node quadrilateral element, 5-node pentagonal element and 6-node hexagonal element, respectively. The two-level mapping for hexagonal element is shown in figure 2.5.

2. The integration scheme for enriched elements are similar to the scheme given in Ref. [44] except that we define the Wachspress shape function over this arbitrary

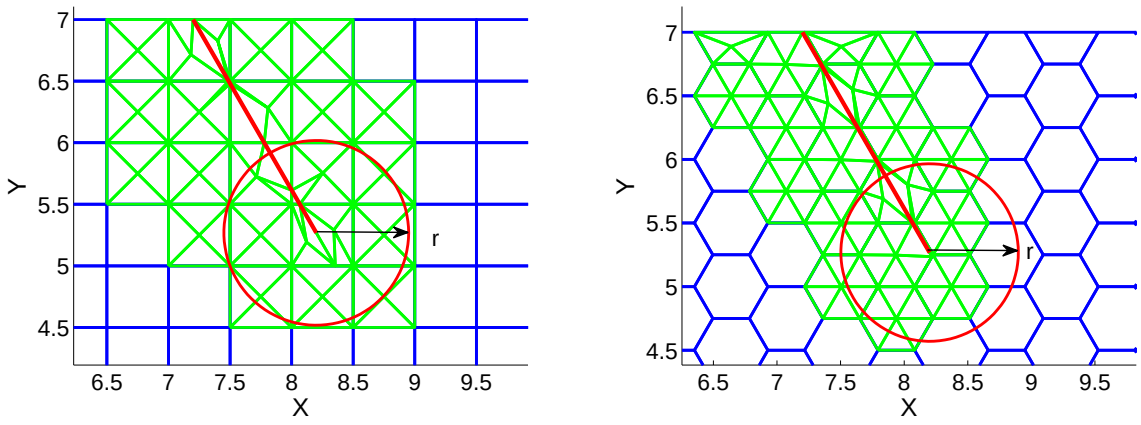

Figure 5.3: Triangulation of enriched elements in (a) quadrilateral and (b) hexagonal structured mesh.

physical element for enriched elements as opposed to on reference polygons in Ref. [44]. Hence the need for mapping the integration points from reference polygon to physical polygon is eliminated as done in Ref. [44]. The actual physical polygonal element is then triangulated. Delaunay triangulation algorithm as implemented in software package TRIPACK [47] is used to triangulate the enriched elements. In each subtriangle a 25-point Gauss quadrature rule is used [42]. Triangulation for enriched elements in quadrilateral and hexagonal mesh is shown in figure 5.3a and figure 5.3b, respectively.

5.4 Numerical Results and Discussions

In this thesis the present method has been applied to edge crack in a plate under uniaxial loading (mode 1) and oblique crack under uniaxial loading (mixed mode) problem. The finite element model with boundary conditions is shown in figure 5.4. Convergence of stress intensity factor with number of nodes has been established. For these problems a quadrilateral and a polygonal mesh have been used and two such meshes are shown in figure (5.5). 2D bars of dimensions L=16, W=7 and a=3.5 for mode 1 problem and L=16, W=7, a=2 and $\beta = 60^o$ for mixed mode problem have been considered. Other

material properties are: $E = 2$ GPa, $\nu = 0.3$ and far field stress $\sigma = 1$ MPa. The reference solution for edge crack in a plate under uniaxial loading is given by [48]

$$K = F(\frac{a}{W})\sigma\sqrt{\pi a} \tag{5.12a}$$

$$F\left(\frac{a}{W}\right) = 1.12 - 0.231\left(\frac{a}{W}\right) + 10.55\left(\frac{a}{W}\right)^2 - 21.72\left(\frac{a}{W}\right)^3 + 30.39\left(\frac{a}{W}\right)^4 \tag{5.12b}$$

where F is the geometry correction factor.

The geometry factors for stress intensity factors for oblique crack under uniaxial loading are computed from the curves given in Ref. [49].

$$K_I = F_I\sigma\sqrt{\pi a}; \quad K_{II} = F_{II}\sigma\sqrt{\pi a} \tag{5.13}$$

for $\beta = 60^o$

$$F_I = 1.25; \quad F_{II} = 0.3875$$

The domain form of the interaction integral is used to extract the stress intensity factors (SIFs) [50, 48] with a domain radius $r = Rh$ (h is the size of the crack-tip element and is defined as square root of the crack-tip element area). Two different values of J domain factor R, namely $R = 1.5$ and $R = 2.0$ are considered. Details on the extraction of SIFs in the X-FEM can be found in Ref. [4].

We use three different methods to compare the convergence of stress intensity factors. All the three methods use triangulation scheme for integration over enriched elements. The methods differ only in terms of use of integration scheme for unenriched elements. In Method 1 we use standard isoparametric mapping with 2×2 Guass integration in structured quadrilateral finite element mesh. In Method 2 we use optimal integration scheme with SC mapping in structured quadrilateral finite element mesh. In method 3 we use optimal integration scheme with SC mapping for structured hexagonal finite element mesh.

Figure 5.6a shows the convergence of three different methods for $R = 1.5$ for pure mode 1 case. Method 3, that is the optimal integration scheme applied over hexagonal

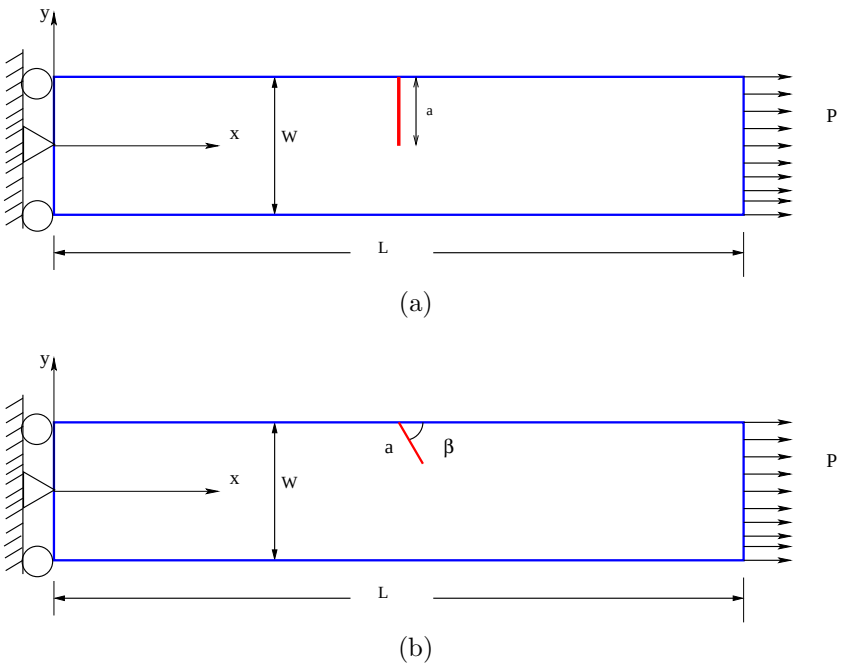

Figure 5.4: Finite element model with boundary conditions. (a) Edge crack. (b) Oblique crack.

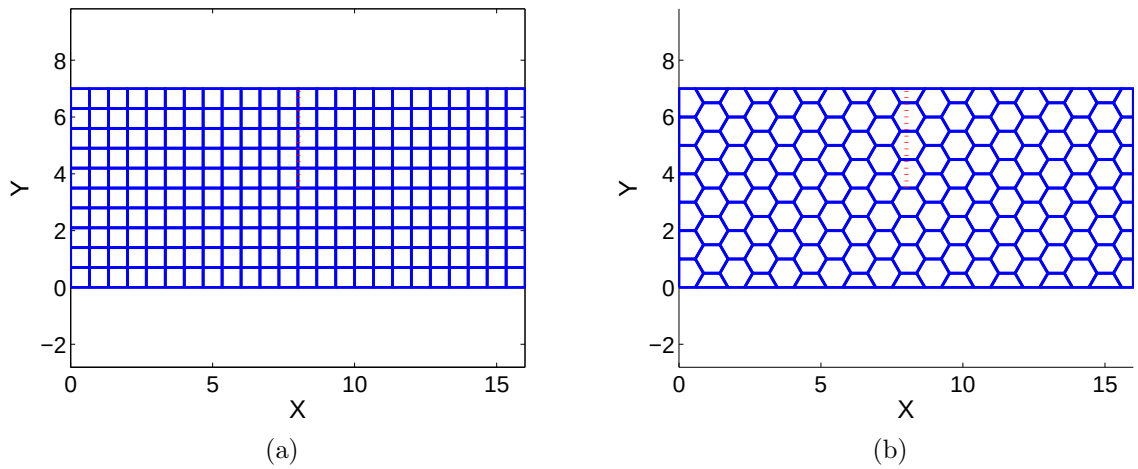

Figure 5.5: (a) Quadrilateral and (b) hexagonal structured mesh.

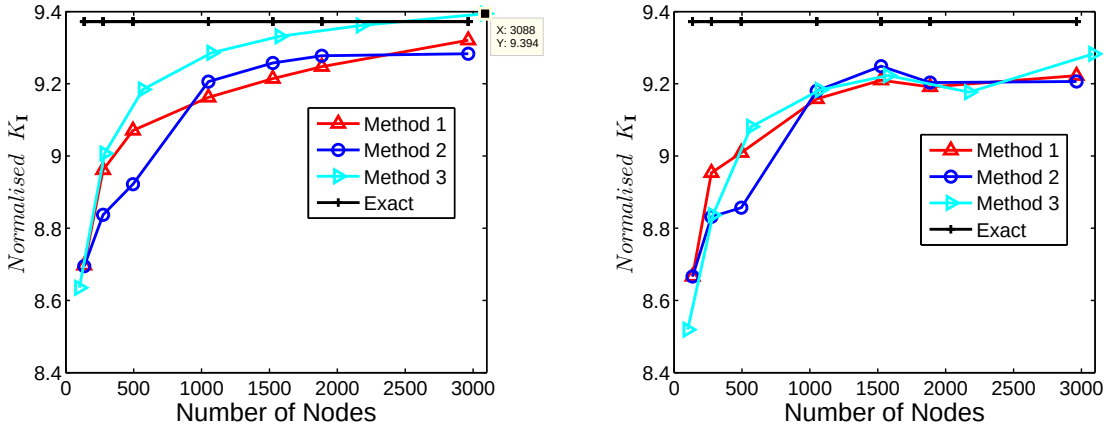

Figure 5.6: Convergence in mode 1 SIF for edge crack under uniaxial loading for (a) R = 1.5. (b) R = 2.0.

mesh displays faster convergence when compared to two other methods. However in case of factor $R = 2.0$ (fig. 5.6b) all the three methods shows more of less similar kind if trends.

Figure 5.7 shows the convergence of mode 1 and mode 2 stress intensity factors for the mixed mode problem. Figures 5.7a and 5.7b shows the convergence of mode 1 and mode 2 stress intensity factors with number of nodes, respectively. Here too the Method 3 shows better convergence rate compared to two other methods. Almost similar kind of results observed for factor $R = 2.0$. However, in latter case the oscillations in convergence curves are small compared to the former. This might be due to the fact that stress gradients are very high near crack tip. Hence as the J domain radius is increased J integral becomes more and more smooth.

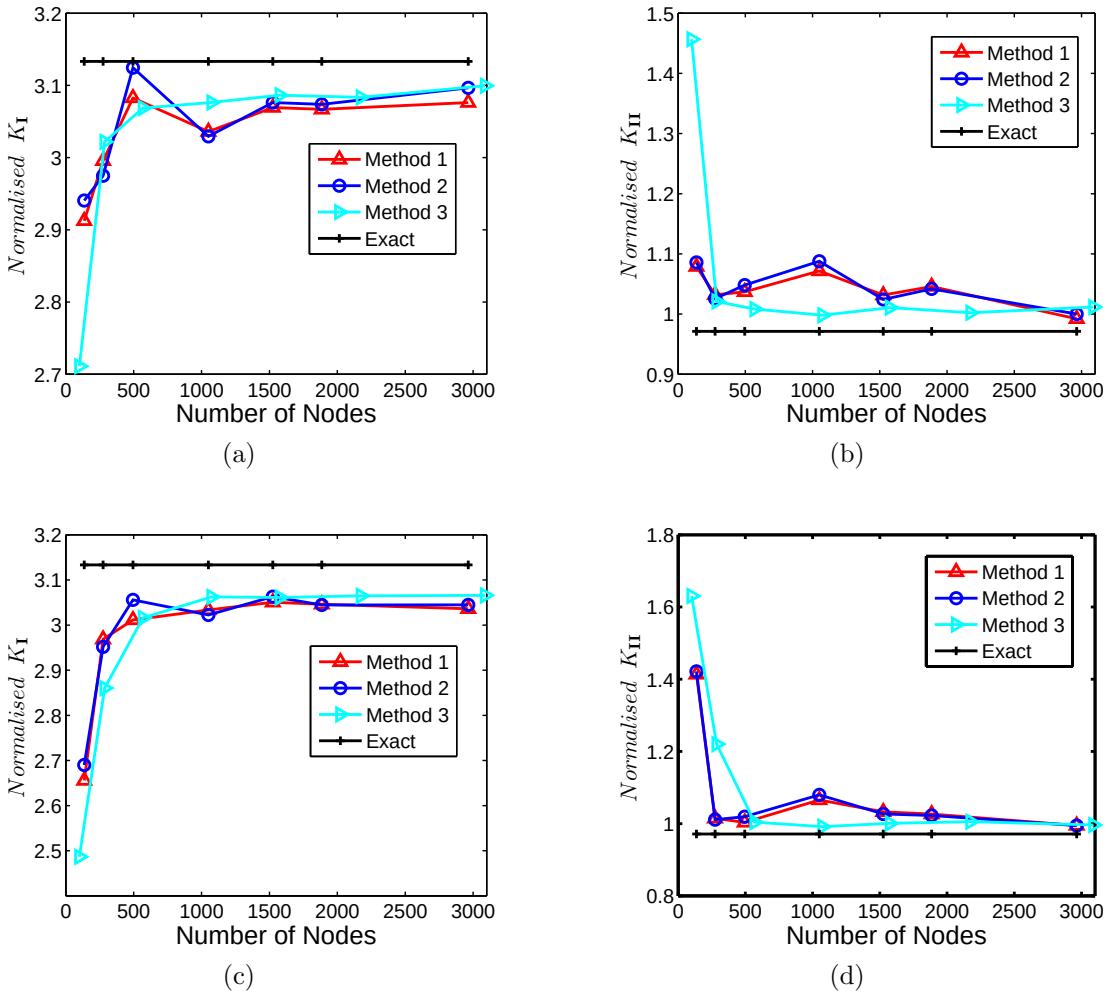

Figure 5.7: Convergence in mixed mode SIFs for oblique crack under uniaxial loading. (a) K_I for R = 1.5. (b) K_{II} for R = 1.5. (c) K_I for R = 2.0. (d) K_{II} for R = 2.0.

Chapter 6

Application of XFEM to Study the Propagation of Crack

6.1 Limitation of FEM in the Crack Propagation Type Problem

Prediction of crack propagation is very crucial in the life prediction of any engineering component. In FEM singular crack tip elements are used for simulation of crack propagation. This implementation requires the crack to coincide with element boundary and crack tip should fall on the node, which complicates the task of remeshing. And when crack propagates this remeshing becomes inevitable. Which cause very high computational cost. In the extended finite element method(XFEM) the generalized heviside function and asymptotic crack-tip enrichment functions are incorporated to conform to the displacement discontinuity due to the crack and eliminates any need of remeshing due to crack propagation.

6.2 Criteria for Crack propagation

For a given crack problem, a criterion is first needed to judge whether the crack is severe enough to propagate or not. If it propagates then in which direction and at what amount it will propagate. Several crack propagation criteria has been proposed as for example maximum energy release rate [51], minimum strain energy density[52] and maximum circumferential stress[53]. In the present work maximum circumferential stress criteria is used. According to this criteria a crack will propagate when the circumferential stress reaches it's critical value . We can write this criteria in terms of SIF values as

$$K_{eq} = K_{ic} \tag{6.1}$$

Where K_{ic} is the material Fracture Toughness(which is unique for a particular material). And K_{eq} is written in terms of K_I and K_{II} as below

$$K_{eq} = K_1 Cos^3(\frac{\theta}{2}) - \frac{3}{2} K_2 Cos(\frac{\theta}{2}) Sin(\theta) \tag{6.2}$$

"θ" is the predicted crack propagation angle, as shown in figure(6.1)

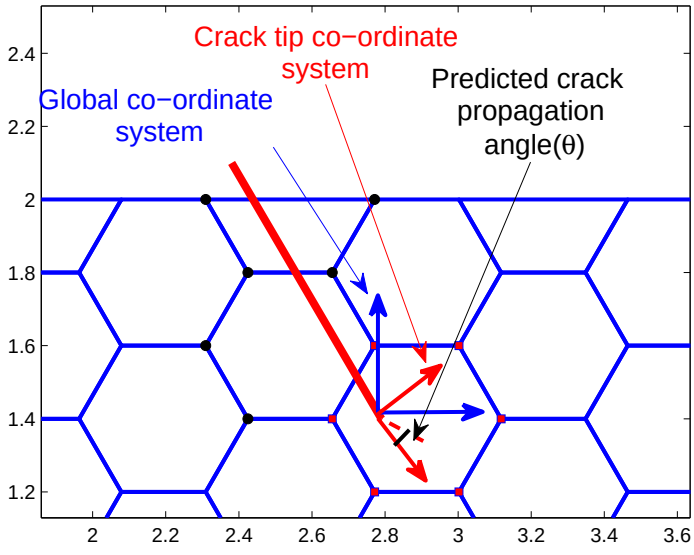

Figure 6.1: Local crack tip co-ordinate system.

6.3 Geometry and Material Property of the Beam Specimen.

For the study of crack propagation we are using a rectangular beam of length(L)=5m, width(W)=2m and thickness(t)=1m with homogeneous isotropic material of Young's Modulas(E) 20 GPa, Poisson's Ratio 0.3 and Fracture Toughness 50MPa$\sqrt{m}$. One end of the beam is fixed and other end is free(cantiliver type). Tesile force of magnitude 1000N is applied at the free end of the beam. Two types of crck has been considered, edge crack and oblique crack. Figure(6.2) shows the boundary condition, crack geometry and applied load on the beam.

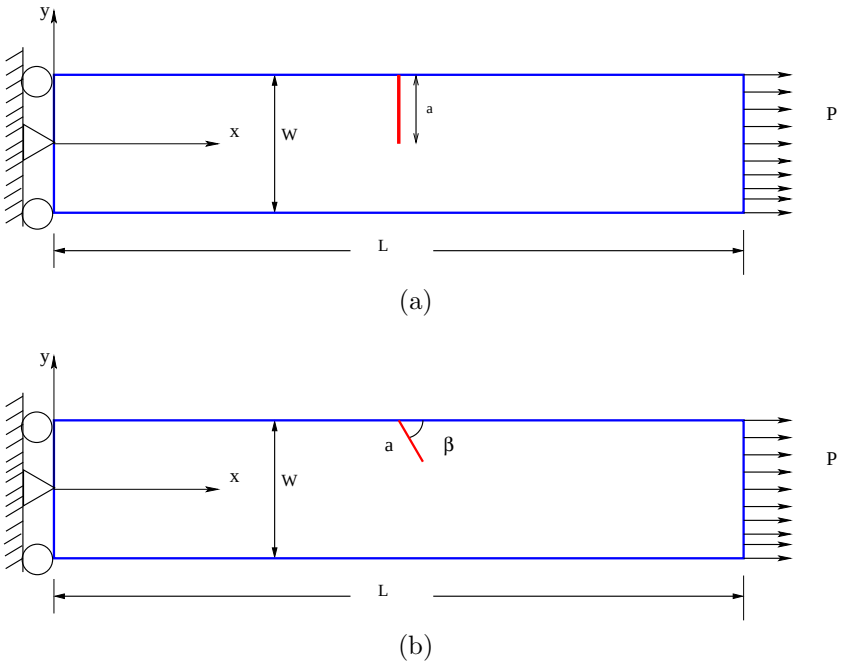

Figure 6.2: Finite element model with boundary conditions. (a) Edge crack. (b) Oblique crack.

S

6.4 Numerical Results and Discussion

Figure(6.3) shows the initial crack geometry and meshing using structured 4 node quadrilateral element.

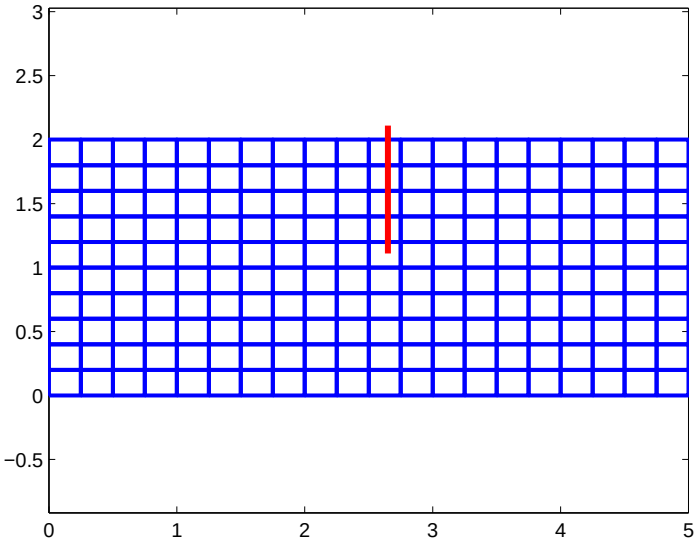

Figure 6.3: Local crack tip co-ordinate system.

Distribution of three different types of stress, namely σ_{xx}, σ_{yy} and σ_{xy} for pure mode I case using structured mesh with 4 node quadrilateral element has been shown in figre(6.4).

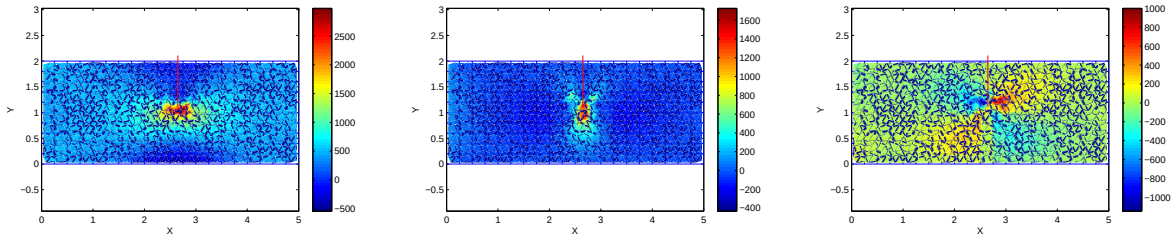

(a) (b) (c)

Figure 6.4: Smoothed(nodal averaging) stress distribution(before crack propagation) for straight edge crack under uniaxial loading for structured mesh using 4 node quadrilateral elements. (a) σ_{xx}. (b) σ_{yy}. (c) σ_{xy}

Figure(6.5) shows the distribution of stresses σ_{xx}, σ_{yy} and σ_{xy} after two steps of crack

propagation.

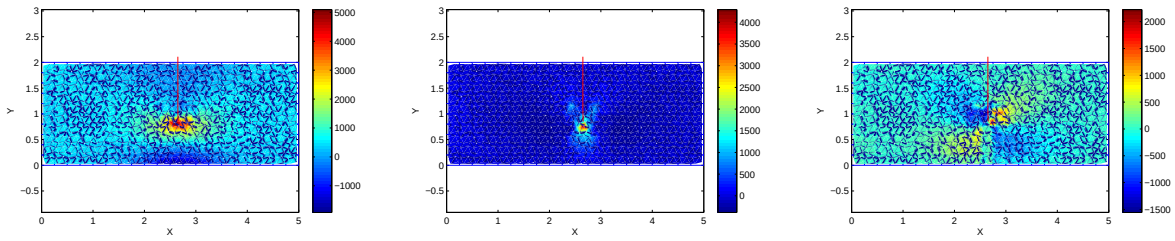

(a) (b) (c)

Figure 6.5: Smoothed(nodal averaging) stress distribution(after two steps of crack propagation) for straight edge crack under uniaxial loading for structured mesh using 4 node quadrilateral elements. (a) σ_{xx}. (b) σ_{yy}. (c) σ_{xy}

Figure(6.6) shows the distribution of stresses σ_{xx}, σ_{yy} and σ_{xy} after five steps of crack propagation.

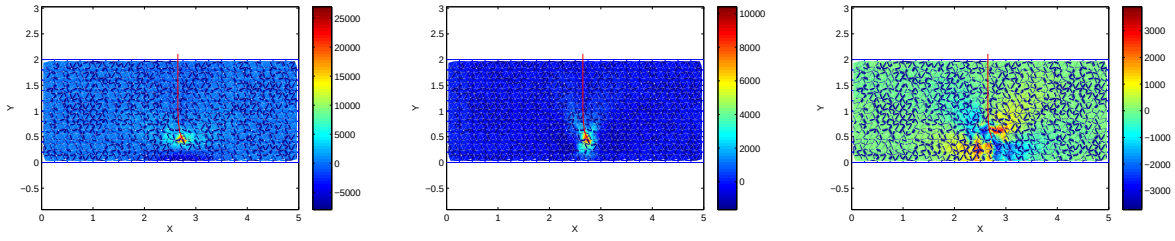

(a) (b) (c)

Figure 6.6: Smoothed(nodal averaging) stress distribution(after five steps of crack propagation) for straight edge crack under uniaxial loading for structured mesh using 4 node quadrilateral elements. (a) σ_{xx}. (b) σ_{yy}. (c) σ_{xy}

Figure(6.7) shows the initial crack geometry and meshing using regular hexagonal element.

Distribution of three different types of stress, namely σ_{xx}, σ_{yy} and σ_{xy} for pure mode I case using structured mesh with 6 node hexagonal element has been shown in figre(6.8).

Figure(6.9) shows the distribution of stresses σ_{xx}, σ_{yy} and σ_{xy} after two steps of crack propagation.

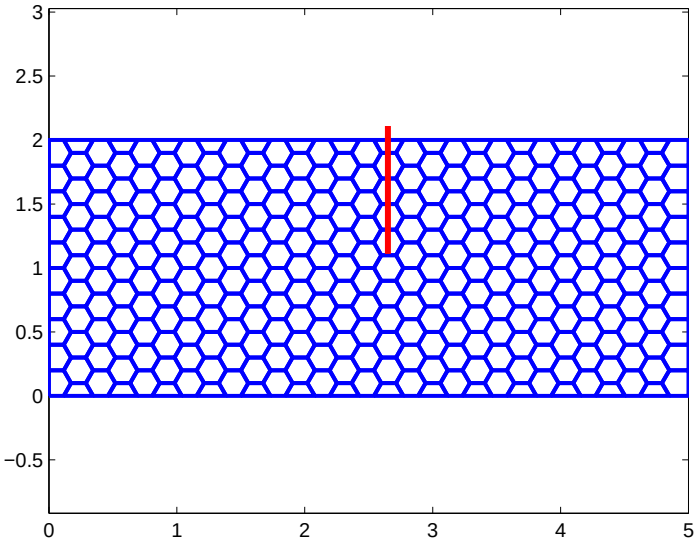

Figure 6.7: Local crack tip co-ordinate system.

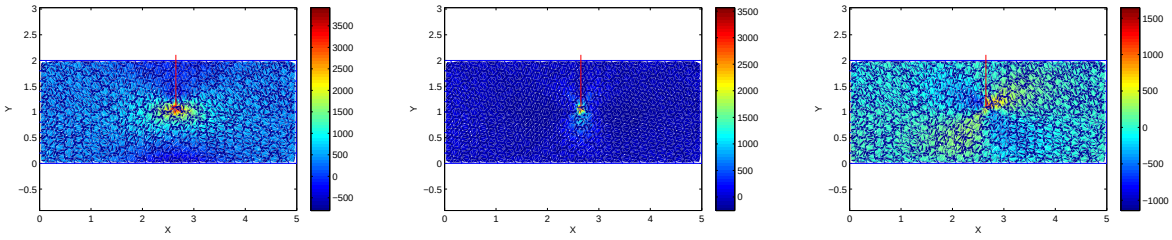

(a) (b) (c)

Figure 6.8: Smoothed(nodal averaging) stress distribution(before crack propagation) for straight edge crack under uniaxial loading for structured mesh using 6 node hexagonal elements. (a) σ_{xx}. (b) σ_{yy}. (c) σ_{xy}

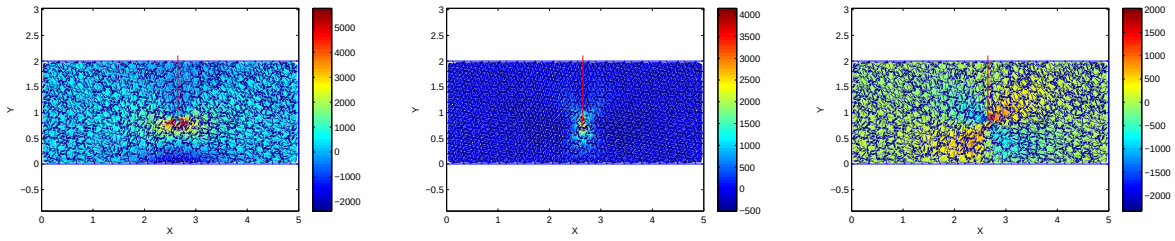

(a) (b) (c)

Figure 6.9: Smoothed(nodal averaging) stress distribution(after two steps of crack propagation) for straight edge crack under uniaxial loading for structured mesh using 6 node hexagonal elements. (a) σ_{xx}. (b) σ_{yy}. (c) σ_{xy}

Figure(6.10) shows the distribution of stresses σ_{xx}, σ_{yy} and σ_{xy} after five steps of crack propagation.

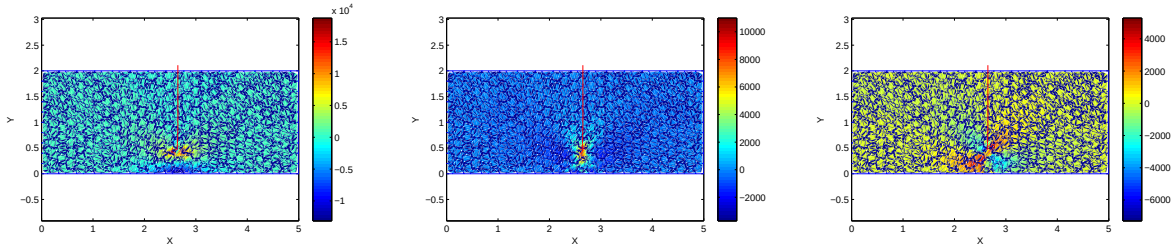

(a) (b) (c)

Figure 6.10: Smoothed(nodal averaging) stress distribution(after five steps of crack propagation) for straight edge crack under uniaxial loading for structured mesh using 6 node hexagonal elements. (a) σ_{xx}. (b) σ_{yy}. (c) σ_{xy}

Figure(6.11) shows the initial crack geometry and meshing using regular quadrilateral element for oblique crack.

Distribution of three different types of stress, namely σ_{xx}, σ_{yy} and σ_{xy} for pure mode II case using structured mesh with 4 node quadrilateral element has been shown in figre(6.12).

Figure(6.13) shows the distribution of stresses σ_{xx}, σ_{yy} and σ_{xy} after two steps of crack propagation.

Figure(6.14) shows the distribution of stresses σ_{xx}, σ_{yy} and σ_{xy} after five steps of crack

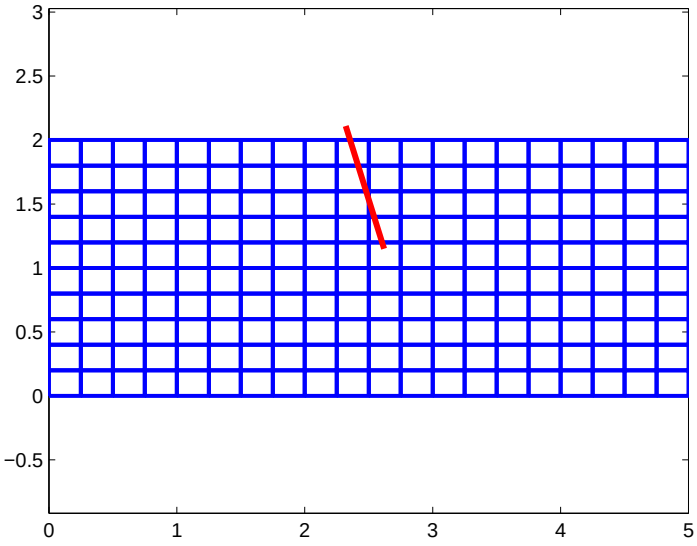

Figure 6.11: Local crack tip co-ordinate system.

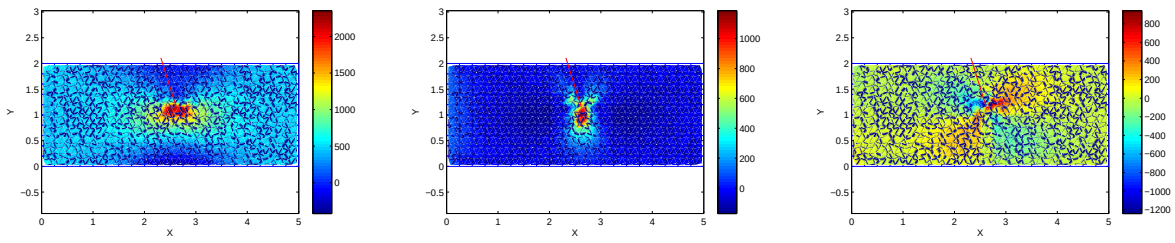

(a) (b) (c)

Figure 6.12: Smoothed(nodal averaging) stress distribution(before crack propagation) for oblique crack under uniaxial loading for structured mesh using 4 node quadrilateral elements. (a) σ_{xx}. (b) σ_{yy}. (c) σ_{xy}

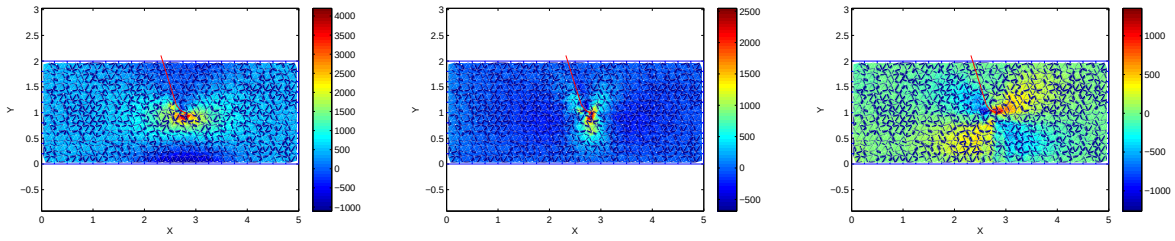

(a) (b) (c)

Figure 6.13: Smoothed(nodal averaging) stress distribution(after two steps of crack propagation) for oblique crack under uniaxial loading for structured mesh using 4 node quadrilateral elements. (a) σ_{xx}. (b) σ_{yy}. (c) σ_{xy}

propagation.

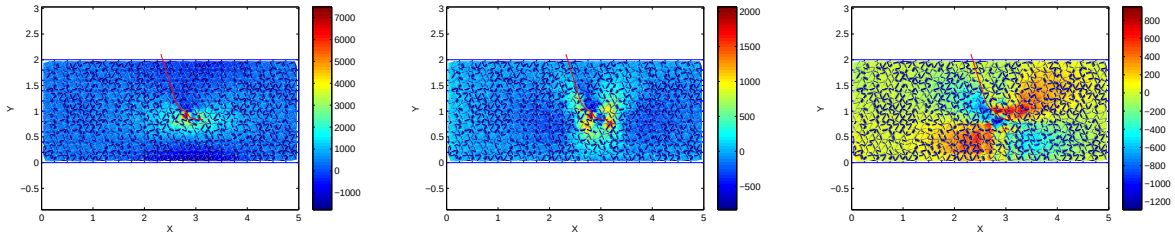

(a) (b) (c)

Figure 6.14: Smoothed(nodal averaging) stress distribution(after five steps of crack propagation) for oblique crack under uniaxial loading for structured mesh using 4 node quadrilateral elements. (a) σ_{xx}. (b) σ_{yy}. (c) σ_{xy}

Figure(6.15) shows the initial crack geometry and meshing using regular hexagonal element.

Distribution of three different types of stress, namely σ_{xx}, σ_{yy} and σ_{xy} for pure mode II case using structured mesh with 6 node hexagonal element has been shown in figre(6.16).

Figure(6.17) shows the distribution of stresses σ_{xx}, σ_{yy} and σ_{xy} after two steps of crack propagation.

Figure(6.18) shows the distribution of stresses σ_{xx}, σ_{yy} and σ_{xy} after five steps of crack propagation.

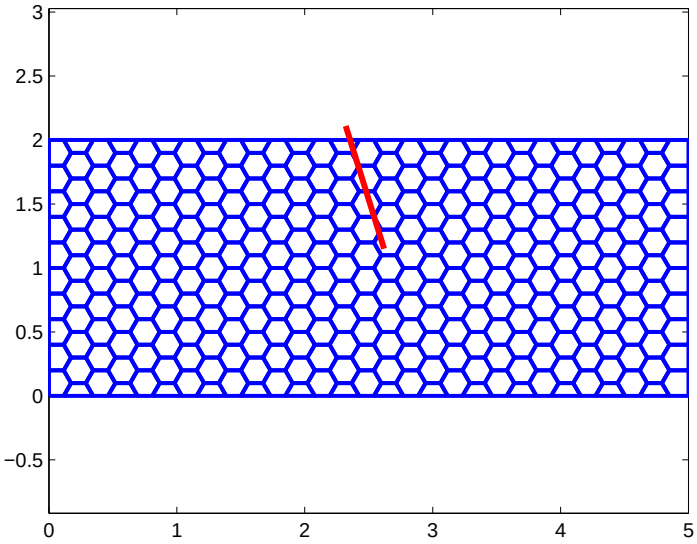

Figure 6.15: Local crack tip co-ordinate system.

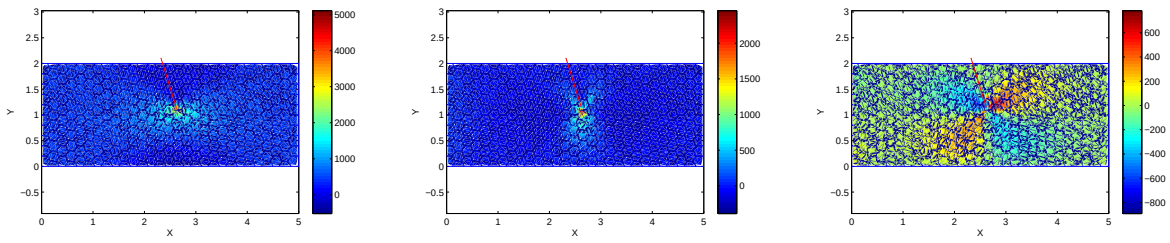

(a) (b) (c)

Figure 6.16: Smoothed(nodal averaging) stress distribution(before crack propagation) for oblique crack under uniaxial loading for structured mesh using 6 node hexagonal elements. (a) σ_{xx}. (b) σ_{yy}. (c) σ_{xy}

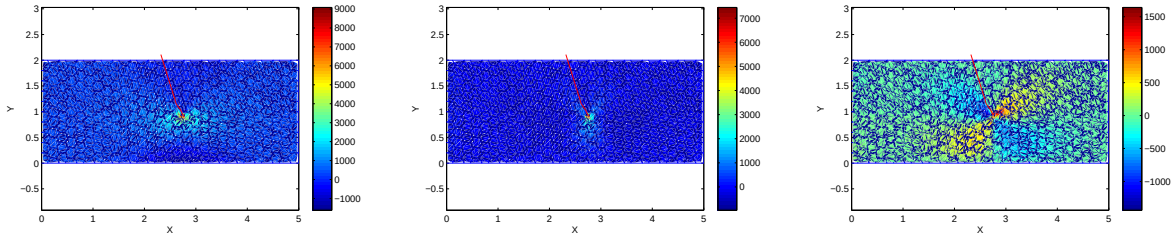

(a) (b) (c)

Figure 6.17: Smoothed(nodal averaging) stress distribution(after two steps of crack propagation) for oblique crack under uniaxial loading for structured mesh using 6 node hexagonal elements. (a) σ_{xx}. (b) σ_{yy}. (c) σ_{xy}

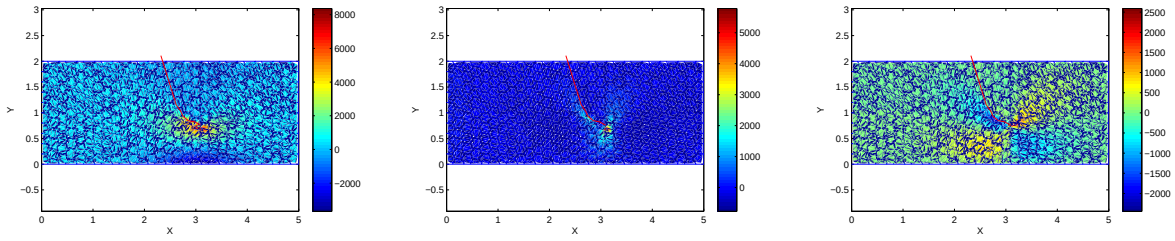

(a) (b) (c)

Figure 6.18: Smoothed(nodal averaging) stress distribution(after five steps of crack propagation) for oblique crack under uniaxial loading for structured mesh using 6 node hexagonal elements. (a) σ_{xx}. (b) σ_{yy}. (c) σ_{xy}

From the above results it is clear that in case of edge crack(mode-I) crack is propagating through the same path for both quadrilateral and hexagonal mesh and also it remains almost verticle, as predicted. And in case of oblique crack(mixed mode) both quadrilateral and hexagonal mesh shows similar pattern in the propagation of crack.

Chapter 7

Conclusions and Future Work

7.1 Summary of the Completed Work and Scope of Future Work

A new integration scheme has been implemented to study the the problem of linear elasticity with polygonal framework without dividing the polygons further into triangle or quadrilateral. Extra integration points has been used near the element boundary so that next when some smoothing function will be used for smooth variation of the material property across the element these extra integration points near the boundary will incorporate that effect into the problem. Till now only quadrilateral, pentagonal and hexagonal elements have been used as a polygonal element but these need to be extended for polygon with more number of sides because grains of the polycrystalline material can be a polygon of quite high number of sides though any polygon with large number of sides can be subdevided into polygon with lower number of sides. In the fracture mechanics the problems have been studied for mode-I and mixed mode crack. But the one limitation is that cack should not pass along the element boundary and crack tip should not fall on the node. But in polycrystalline types of material the element boundaries are the most weakest zone and crack is mos likely to pass along the element boundary. This limitation has to be removed. In the present work crack branching and

microcracking and coalition of multiple crack has not been considered. These effects have to be incorporated to study the intergranular and intragranular propagation of crack in polycrystalline material effectively.

Bibliography

[1] Chan SK, Tuba IS, Wilson WK. On finite element method in linear fracture mechanics. *Engineering Fracture Mechanics* 1970; **2**:1–17.

[2] Li FZ, Shih CF, Needleman A. A comparison of methods for calculating energy release rates. *Engineering Fracture Mechanics* 1985; **21**(2):405–421.

[3] Belytschko T, Black T. Elastic crack growth in finite elements with minimal remeshing. *International Journal for Numerical Methods in Engineering* 1999; **45**:601–620.

[4] Moës N, Dolbow J, Belytschko T. A finite element method for crack growth without remeshing. *International Journal for Numerical Methods in Engineering* 1999; **46**:131–150.

[5] Dolbow JE. An extended finite element method with discontinuous enrichment for applied mechanics. PhD dissertation, Theoretical and Applied Mechanics, Northwestern University, USA.

[6] Natarajan S, Mahapatra DR, Bordas S. Integrating strong and weak discontinuities without integration subcells and example applications in an XFEM/GFEM framework. *International Journal for Numerical Methods in Engineering* 2010; Article in Press. DOI: 10.1002/nme. 2798.

[7] Liu GR, Dai KY, Nguyen TT. A smoothed finite element for mechanics problems. *Computational Mechanics* 2007; **39**(6): 859–877.

[8] Chen JS, Wu CT, Yoon S, You Y. A stabilized conforming nodal integration for Galerkin mesh-free methods. *International Journal for Numerical Methods in Engineering* 2001; **50**:435–466.

[9] Natarajan S, Bordas S, Mahapatra DR, Pont SD, Rabczuk T, Noel D, Guo Z. On the smoothed extended finite element method. *International Journal for Numerical Methods in Engineering* 2009; **00**:1–6.

[10] Bordas S, Rabczuk T, Hung N, Nguyen VP, Natarajan S, Bog T, Quan DM, Hiep NV. Strain smoothing in FEM and XFEM. *Computers & Structures* 2008; Article in Press. DOI:10.1016/j.compstruc.2008.07.006.

[11] Wachspress EL. A rational basis for function approximation. *Lecture notes in Mathematics*; 1971.

[12] Malsch EA, Dasgupta G. Shape functions for polygonal domains with interior nodes. *International Journal for Numerical Methods in Engineering* 2004; **61**:1153-1172.

[13] Sukumar N, Tabarraei A. Conforming polygonal finite elements. *International Journal for Numerical Methods in Engineering* 2004; **61**:2045–2066.

[14] Meyer M, Lee H, Barr AH. Generalized barycentric coordinates for irregular n-gons. *Journal of Graphics Tools* 2002; **7**(1):13–22.

[15] Floater MS. Mean value coordinates. *Computer Aided Geometric Design* 2003; **20**:19-27.

[16] Sukumar N, Malsch EA. Recent advances in the construction of polygonal finite element interpolants. *Archives of Computational Methods in Engineering* 2006; **13**(1):129–163.

[17] Sukumar N. Construction of polygonal interpolants: A maximum entropy approach. *International Journal for Numerical Methods in Engineering* 2004; **61**(12):2159–2181.

[18] Nguyen VP, Rabczuk T, Bordas S, Duflot M. Meshless methods: A review and computer implementation aspects. *Mathematics and Computers in Simulation* 2008; **79**(3):763–813.

[19] Wandzura S, Xiao H. Symmetric quadrature rules on a triangle. *Computers and Mathematics with Applications* 2003; **45**:1829-1840.

[20] Natarajan S, Bordas SP, Mahapatra DR. Numerical integration over arbitrary polygonal domains based on schwarz-christoffel conformal mapping. *International Journal for Numerical Methods in Engineering* 2009; **80**:103–134.

[21] Suvranu D, Bathe KJ. The method of finite spheres with improved numerical integration. *Computers and structures* 2001; **79**(1).

[22] Dasgupta Gautam. Interpolants within convex polygons: Wachspress' shape functions. *ASCE - Journal of aerospace engineering* 2003; **16**:1–8.

[23] Cueto E, Sukumar N, Calvo B, Martínez MA, Cegoñino J, Doblaré M. Overview and recent advances in natural neighbour galerkin methods. *Archives of Computational Methods in Engineering* 2003; **10**(4):307–384.

[24] Sukumar N, Moran B, Belytschko T. The natural element method in solid mechanics. *International Journal for Numerical Methods in Engineering* 1998; **43**(5):839–887.

[25] Arroyo M, Ortiz M. Local Maximum-entropy Approximation Schemes. *Lecture Notes in Computational Science and Engineering,* vol. 57 Springer: Berlin, 2006; 1-16.

[26] Arroyo M, Ortiz M. Local maximum-entropy approximation schemes: a seamless bridge between finite elements and meshfree methods. *International Journal for Numerical Methods in Engineering* 2006; **65**(13):2167-2202.

[27] Sukumar N. Maximum entropy approximation. *Bayesian Inference and Maximum Entropy Methods in Science and Engineering* 2005; **803**:337344.

[28] Sukumar N, Wright R. Overview and construction of meshfree basis functions: from moving least squares to entropy approximants. *International Journal for Numerical Methods in Engineering* 2007; **70**:181-205.

[29] Warren J, Schaefer S, Hirani A, Desbrun M. Barycentric coordinates for convex sets. *Advances in Computational Mechanics* 2007; **27**(3):319–338.

[30] Zwiluncer D. *CRC Standard Mathematical Tables and Formulae,* (31st edn) Chapman & Hall/CRC:2003.

[31] Warren J. On the uniqueness of barycentric coordinates. *Contemporary Mathematics: Proceedings of AGGM02* 2003; :93–99.

[32] Nguyen-Xuan H, Bordas S, Nguyen-Dang H. A smoothed finite element method for shells. *Computer Methods in Applied Mechanics and Engineering* 2008; **198**:165–177.

[33] Chen JS, Wang HP. Some recent improvements in meshfree methods for incompressible finite elasticity boundary value problems with contact. *Computational Mechanics* 2000; **25**:137–156.

[34] Bordas S, Natrajan S. On the approximation in the smoothed finite element method. *International Journal for Numerical Methods in Engineering* 2010; **81**:660–670.

[35] Mousavi SE, Xiao H, Sukumar N. Generalized Gaussian quadrature rules on arbitrary polygons. *International Journal for Numerical Methods in Engineering* 2010; **82**:99–113.

[36] Trefethen LN, Numerical computation of the schwarz-christoffel transformation. *SIAM Journal of Scientific and Statistical Computing* 1980; **1**:82–102.

[37] Driscoll TA, Trefethen LN. Algorithm 756: a matlab tool box for Schwarz Christoffel mapping. *ACM Transactions on Mathematical Software* 1996; **22**(2):168-186.

[38] Driscoll TA, Trefethen LN. Schwarz-Christoffel mapping. *Cambridge Monographs on Applied and Computational Mathematics* 2002; **8**(1).

[39] Timoshenko SP, Goodier JN. *Theory of Elasticity,* McGraw-Hill: New York: 1970.

[40] Augarde CE, Deeks AJ. The use of Timoshenkos exact solution for a cantilever beam in adaptive analysis. *Finite Elements in Analysis and Design* 2008; **44**:595–601.

[41] Golub GH, Loan CFV. *Matrix Computations,* (3rd edn) The John Hopkins University Press:Baltimore and London:1996; 58–59.

[42] Dunavant DA. High degree efficient symmetrical Guassian quadrature rules for the triangle. *International Journal for Numerical Methods in Engineering* 1985; **21**:1129–1148.

[43] Babuska I, Melenk JM. The partition of unity method. *International Journal for Numerical Methods in Engineering* 1997 **40**:727–758

[44] Tabarraei A, Sukumar N. Extended finite element method on polygonal and quadtree meshes. *Computer Methods in Applied Mechanics and Engineering* 2007; **197**:425–438.

[45] Singh S, Natarajan S, Mahapatra DR, Bordas S. Optimal numerical integration schemes for polygonal finite elements. *International Journal for Numerical Methods in Engineering* 2010; Paper under review.

[46] Mohammadi S. *Extended Finite Element Method,* (1st edn) Blackwell Publishing:2008

[47] Renka RJ, Algorithm 751: TRIPACK, A constrained two-dimensional Delaunay triangulation package, *ACM Transactions on Mathematical Software* 1996; **22**(1):1–8

[48] Gdoutos EE. *Fracture Mechanics,* Kluwer Academics Publishers:1993 Boston.

[49] Murakami Y. *Stress Intensity Factors Handbook,* Pergamon Press:1987 Oxford.

[50] Yau J, Wang S, Corten H. A mixed-mode crack analysis of isotropic solids using conservation laws of elasticity. *Journal of Applied Mechanics* 1980; **47**:335–341.

[51] Hussain MA,Pu SL,Underwood JH Strain energy release rate for a crack under combined mode-I and mode-II,fracture analysis *ASTMSTP560,Philadelphia* 1974 2-8;

[52] Sih GC, Macdonald B. Fracture mechanics applied to engineering problems - strain energy density fracture criterion *Eng. Fract. Mech* 1974 **6**:361-386

[53] Erdogan F,Sih GC. On the crack extension in plane loading and transverse shear. *J. Basic Eng.* 1963 **85**:519-27

[54] Torsten Luther, Carsten Knke. Polycrystal models for the analysis of intergranular crack growth in metallic materials. *Eng. Fract. Mech.* 2009 76:2332-2343 **85**:519-27